CANCER

Clonal cooperation through soluble metabolite exchange facilitates metastatic outgrowth by modulating Allee effect

Benjamin J. Hershey[1], Sara Barozzi[1], Fabrizio Orsenigo[1], Simone Pompei[1], Fabio Iannelli[1], Stephan Kamrad[2], Vittoria Matafora[1], Federica Pisati[3], Ludovico Calabrese[1], Giuseppe Fragale[1], Giulia Salvadori[1], Emanuele Martini[1], Maria Grazia Totaro[1], Serena Magni[1], Rui Guan[2], Dario Parazzoli[1], Paolo Maiuri[4], Angela Bachi[1], Kiran R. Patil[2], Marco Cosentino Lagomarsino[1,5], Kristina M. Havas[1]*

Cancers feature substantial intratumoral heterogeneity of genetic and phenotypically distinct lineages. Although interactions between coexisting lineages are emerging as a potential contributor to tumor evolution, the extent and nature of these interactions remain largely unknown. We postulated that tumors develop ecological interactions that sustain diversity and facilitate metastasis. Using a combination of fluorescent barcoding, mathematical modeling, metabolic analysis, and in vivo models, we show that the Allee effect, i.e., growth dependency on population size, is a feature of tumor lineages and that cooperative ecological interactions between lineages alleviate the Allee barriers to growth in a model of triple-negative breast cancer. Soluble metabolite exchange formed the basis for these cooperative interactions and catalyzed the establishment of a polyclonal community that displayed enhanced metastatic dissemination and outgrowth in xenograft models. Our results highlight interclonal metabolite exchange as a key modulator of tumor ecology and a contributing factor to overcoming Allee effect–associated growth barriers to metastasis.

INTRODUCTION

Genetic and phenotypic heterogeneity has emerged as a hallmark of almost all malignancies and has been shown to contribute to tumor establishment and progression (*1*–*5*). It was recently demonstrated that genetic and phenotypic heterogeneity is maintained ex vivo and exists as a constantly evolving feature of tumor cell lines (*6*). This challenges the simple evolutionary model leading to the dominance of a single clone both in the regime of selective sweep and in neutral conditions. However, more complex scenarios with frequency-dependent phenomena take place, even in simplified settings. For example, chemostat-based studies in microbial systems suggest that even in a stirred continuous culture ecological interactions act as a mechanism for stabilizing diversity in evolving populations (*7*). These studies support the idea that interactions like cross-feeding can evolve even in the presence of a simple fitness constraint: selection of faster growth. Furthermore, establishment of ecological interactions does not preclude further evolution, as demonstrated in the pioneering work done by Lenski and colleagues (*8*), in which *Escherichia coli* tracked over 60,000 generations evolved into stably existing ecotypes with continual evolution within each clade. While the generational times and phenotypes may differ greatly between microbial and tumor systems, both operate within the overall variation-selection regime. Several lines of evidence demonstrate that it is likely that tumor progression could be supported through the establishment of such cooperative or syntrophic interactions between phenotypically distinct clonal populations (*9*–*12*). Additionally, in vivo and ex vivo observations of heterogeneity within tumor cell populations (*1*–*6*, *13*) support the hypothesis that interclone interactions could help maintain clonal diversity and contribute to the collective fitness of a tumor.

Intratumoral interactions could be most critical at specific moments during tumorigenesis such as initiation and metastasis. These settings are characterized by tumor growth at low densities, rendering it important to consider the contribution of such interactions on Allee effect–imposed thresholds to growth. The Allee effect is an ecological phenomenon whereby there is a positive correlation between individual fitness and average population size or density (*14*, *15*). This effect is most critical in regimes of low density, such as those found during cancer initiation, invasion, and metastasis. Yet, by undetermined means, tumors and metastases are able to overcome this antagonistic effect and reach establishment. However, these settings are often overlooked in traditional models of tumors, and the joint contributions of Allee effect and ecological interactions to tumor onset and progression and the mechanisms by which tumors evade Allee thresholds to growth remain relatively unstudied.

Here, to test whether tumors use division of labor to optimize overall fitness, we use breast cancer cell lines representative of triple-negative, luminal A, and Her2$^+$ breast cancers that are characterized by high levels of genetic diversity. We demonstrate that ecological interactions between distinct lineages found within cancer cell lines contribute to individual fitness, and that these interactions are a hallmark of karyotypically diverse cancer cell lines. The results suggest that tumors emerge by overcoming a weak Allee effect, which is alleviated by cooperative ecological interactions among phenotypically distinct subpopulations. We found that interactions are mediated by soluble metabolite exchange between

[1]IFOM ETS The AIRC Institute of Molecular Oncology, Milan, Italy. [2]Medical Research Council Toxicology Unit, Cambridge, UK. [3]Histopathology Unit, Cogentech S.C.A.R.L., Milan, Italy. [4]University of Naples Federico II, Naples, Italy. [5]University of Milano, Milan, Italy.
*Corresponding author. Email: kristina.havas@ifom.eu

the constituent lineages, which build the subpopulations. Through the isolation of a minimal interacting community, we demonstrate that clonal cooperation by way of soluble factor exchange is a contributing factor to overcoming Allee effect–associated growth barriers in metastatic outgrowth.

RESULTS

Clonal diversity contributes to tumor fitness through positive interclonal interactions

To investigate the potential for ecological interactions to contribute to mean population fitness, we selected a panel of breast cancer cell lines: BT474, MDA-MB-231, and MCF7 representative of HER2$^+$, basal-B/triple-negative (*16*), and estrogen receptor–positive (ER$^+$) breast cancer subtypes, respectively. The near-euploid RPE1-hTert cell line was used as a healthy control. Metaphase spreads were performed to confirm the karyotypic variations between the cell lines (Fig. 1A and data S1). A fundamental hallmark of communities sustained by strong interactions is the inability of any single member to grow in isolation. Therefore, we evaluated the colony-forming capacity of single cells in both cell line–dependent medium, supplemented with 10% dialyzed fetal bovine serum (FBS) and 2 mM glutamine, hereon referred to as growth medium, and medium consisting of 70% filtered parental culture–conditioned medium/30% cell line–dependent medium, hereon referred to as conditioned medium, which served as a proxy for their community of origin in terms of secreted proteins and metabolites, but not in terms of cell-to-cell contacts and cell mechanics (Fig. 1B). We found that conditioned medium markedly enhanced the colony formation efficiency for all the three cancer cell lines. In contrast, colony formation in the euploid cell line, RPE1-hTert, was unaffected by conditioned medium exposure (Fig. 1C, fig. S1A, and data S2). We also observed that overall fitness, as quantified by both cell number and colony size, of the resultant colonies was enhanced in the presence of conditioned medium (Fig. 1D and data S2). Together, these data suggest that strong interlineage-positive interactions take place in aneuploid cell lines through soluble factor exchange.

Aneuploidy, and its associated genomic instability, is a particularly prevalent feature in triple-negative breast cancers (TNBCs) harboring *TP53* mutations. The cell line MDA-MB-231 has been reported to harbor high levels of genetic diversity, with a subclonal structure closely resembling TNBC tumors (*6*). Consequently, we chose to focus on this cell line for a detailed investigation of

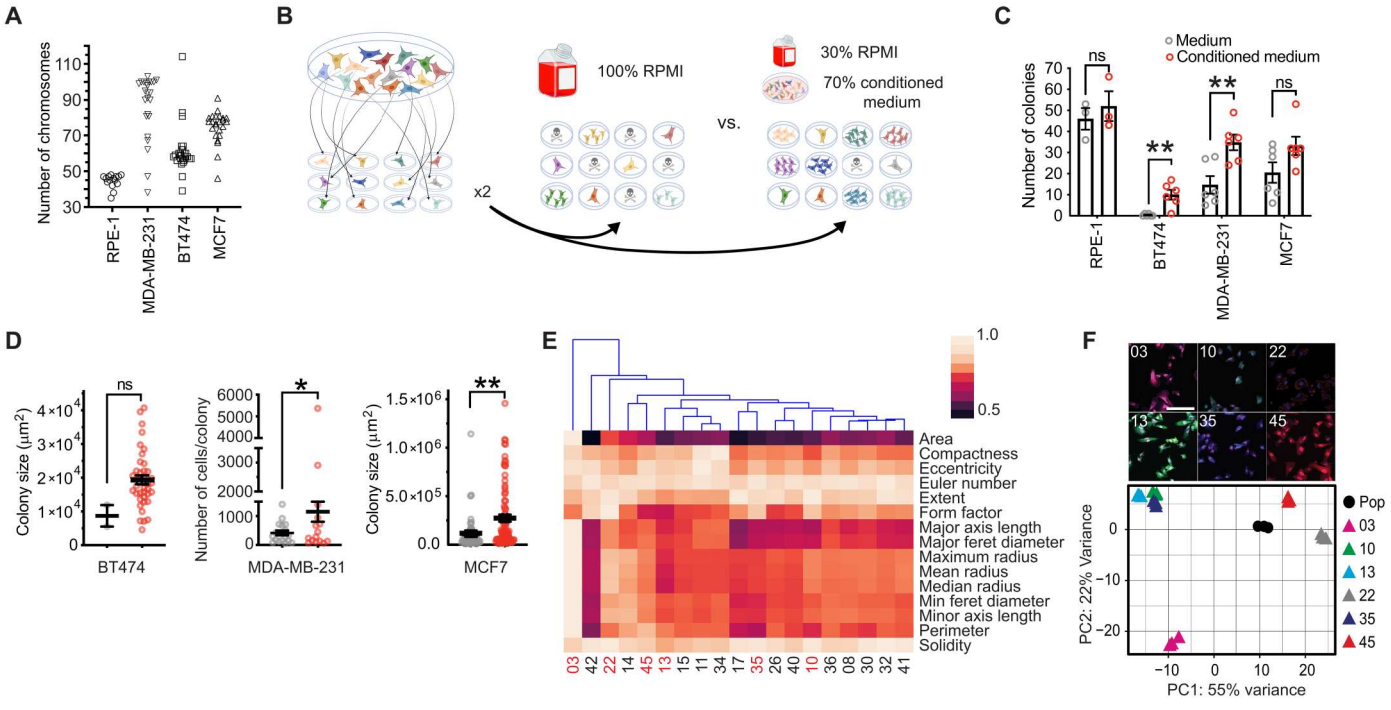

Fig. 1. Soluble factor exchange enhances clonal fitness in multiple breast cancer models. (**A**) Karyotypes of RPE1-hTert ($n = 15$), BT474 ($n = 25$), MDA-MB-231 ($n = 25$), and MCF7 ($n = 24$) cell lines. (**B**) Scheme indicating the design of the single-cell colony formation assay. Cells were seeded at a density of 1.56 cells per cm^2 and maintained in either standard culture medium or a 70:30 mixture of parental culture–conditioned medium:standard medium. Colony number was assessed 16 days after seeding for MDA-MB-231, MCF7, and BT474 cell lines and approximately 8 days after seeding for the RPE1-hTert cell line. (**C**) Number of colonies obtained using the single-cell colony formation assay. A cluster of >10 cells was counted as a colony for the MDA-MB-231, MCF7, and RPE1-hTert cell lines. A clusters of >5 cells was considered a colony for the BT474 cell line. (**D**) Colony fitness as represented by cells/colony approximated by manual counting in ImageJ software for a subset of MDA-MB-231 colonies. The sizes of MCF7 and BT474 colonies were determined by manually defining the colony perimeter and then measuring its area in ImageJ. (**E**) Clustering by morphological features of 19 MDA-MB-231 RGB-derived lineages. Approximately 300 cells per lineage were acquired with a confocal microscope. Morphological parameters were extracted from the images using CellProfiler. (**F**) Confocal images of six morphologically distinct lineages. Scale bar, 100 μm. (Bottom) Principal components analysis of the regularized log-transformed transcriptomic data from six morphologically distinct lineages, 03 (magenta), 10 (green), 13 (sky blue), 22 (gray), 35 (blue), and 45 (red), as well as their parental population (black). Data are represented as mean ± SEM. Significance was determined in Prism 9 using a two-tailed Student's *t* test. *$P < 0.05$, **$P < 0.01$, ***$P < 0.001$, ****$P < 0.0001$.

interlineage interactions. To investigate the contribution of individual lineages to population fitness, we used RGB marking, which allowed both in vitro and in vivo lineage tracing (fig. S1B) (*17*, *18*). Nineteen single-cell clones were isolated from the RGB barcoded MDA-MB-231 cell line grown in parental population conditioned medium. It has been previously demonstrated that clonal morphology is a stable heritable trait that can be used as a distinguishing feature (*19*). Therefore, taking advantage of the color profiles conferred by RGB labeling, along with 4′,6-diamidino-2-phenylindole (DAPI) for nuclear marking, we imaged approximately 400 cells from each of the 19 clonal populations. Using cell profiler, we extracted metrics related to their morphologies and grouped them according to their unique features (Fig. 1E and data S3) (*20*). Six representative lineages from each morphological subgroup, with distinct color profiles, were then selected (Fig. 1F). Transcriptional profiling of the six lineages confirmed that they represent distinct populations (Fig. 1F). The isolation and propagation of these six distinct lineages provided us with the necessary tools to investigate the factors underlying the fitness advantage conferred by population-derived soluble factors.

Maximal growth rate is an emergent property of the tumor and is underpinned by a pervasive weak Allee effect

The most commonly used models of tumor growth are density-independent exponential growth and logistic growth, which is an exponential growth model limited by the carrying capacity of the system. As the six lineages were selected based on the ability of conditioned medium to enhance growth from a single cell, we began by asking whether cell density affected growth rates in the parental population. By calculating doubling times of cells seeded at densities of N_0 = 625 cells/cm^2 and N_0 = 6250 cells/cm^2, we observed a pronounced density dependency to cell growth, with a departure from exponential growth at low densities and increased growth rates at higher densities (fig. S1C and data S4). This behavior deviates from exponential or logistic growth and is referred to as the Allee effect (*14*). A weak Allee effect is defined by slow growth at low inoculum sizes (*15*, *21*, *22*). There are many mechanisms that can give rise to Allee effects, but for a clonally expanding population, shared goods is one of the likely candidates (*23*). In line with this, population-derived conditioned medium improved growth for both seeding densities, virtually extinguishing the Allee effect (fig. S1C). Together, these data suggest that Allee effect is present in the population, and that cooperation through soluble factor exchange could have a role in alleviating it at low densities.

Although often overlooked, understanding ecological regulation of tumor growth kinetics at low densities is fundamental to gaining understanding of tumor initiation, metastatic outgrowth, response to therapy, and reawakening/recurrence (*24*, *25*). To further investigate this phenomenon, we implemented a semi high-throughput growth screen using an Operetta high-content imaging system (Fig. 2A). Briefly, cells were sorted into 96-well plates, fed with either RPMI or parental population conditioned medium, and subsequently imaged at three time points: 6, 24, and 48 hours after seeding, using the nuclear marker SiR-DNA to facilitate cell identification. This system allowed us to accurately assess the growth as a function of population size across a wide range of cell densities: N ranging from 63 to 49,866 cells/cm^2 (Fig. 2B and data S5). A Pearson product-moment correlation coefficient was computed to assess the relationship between the RGB MDA-MB-231 parental population′s fitness, as quantified by per capita growth rate, and initial seeding density. The results confirmed a positive and significant correlation between per capita growth rate and population density in RPMI, r = 0.816 (P = 0.048), and a weaker though insignificant (P = 0.170) positive correlation, r = 0.641, in conditioned medium (Fig. 2B and data S5). This could be attributed to the ability of conditioned medium to enhance per capita growth rates at lower densities. Together, these results revealed an association between cell density and overall fitness, which was less strongly correlated when conditioned medium is present. This suggests that soluble factors are able to decouple cell growth from cell density and alleviate the growth barriers set by the observed Allee effects.

When we extended this analysis to each of our six distinct lineages, we observed a positive correlation between per capita growth rate and cell density across the cohort. With the exception of clone 22 (r = 0.798; P = 0.057), the correlation between fitness and seeding density was significant for all clones when grown in RPMI (Fig. 2B). The strength of the correlation differed between the lineages: clone 13 (r = 0.983) > clone 10 (r = 0.943) > clone 3 (r = 0.874) > clone 35 (r = 0.844) > clone 45 (r = 0.831) > population (r = 0.816) > clone 22 (r = 0.798). It has recently been demonstrated that cancer cell lines undergo constant evolution (*6*). Therefore, we asked whether this phenotype was robust over time by replotting early versus late experimental data for each lineage. We found that the lineages retained a notable similarity in the density-dependent growth kinetics across time (fig. S1D and data S5). As for the parental population, conditioned medium increased per capita growth rates and reduced the association between cell density and fitness across the cohort. Although a positive correlation between per capita growth rate and cell density was observed when the cells were grown in conditioned medium, it was significant only in the case of clone 10 (r = 0.893; P = 0.017) (Fig. 2B). These results indicate that the six distinct linages as well as the parental population are subject to a weak Allee effect. Moreover, in line with a shared good hypothesis, population-derived conditioned medium improved growth across all initial seeding densities, effectively reducing the impact of the Allee effect. The fitness benefit bestowed by conditioned medium had the most pronounced effect at the lowest seeding densities. These findings suggest that maximal tumor population growth is an emergent property of the community, and that collective growth is enhanced by lineage-derived soluble factors.

Ecological interactions affect proliferation-migration dichotomy

In the literature on cancer invasion, the proliferation-migration dichotomy, otherwise known as the "go or grow" phenomenon, refers to the reversible phenotype switching between migratory and proliferative states. It has been suggested that energy allocation, or funneling of resources into proliferation and away from migration-associated processes, is one regulator of cell choice (*26*, *27*). Having established that there is an ecological regulation of proliferation at low densities, we then asked whether the cellular choice between migration and proliferation could be equally affected by population-derived soluble factors. To do so, we tested speed and persistence of cell trajectories in random field migration in the presence or absence of population-derived conditioned medium. Consistent with the enhancement of the proliferative properties observed in the presence of conditioned medium, soluble factors slightly, yet significantly, repressed the migratory capacity of the

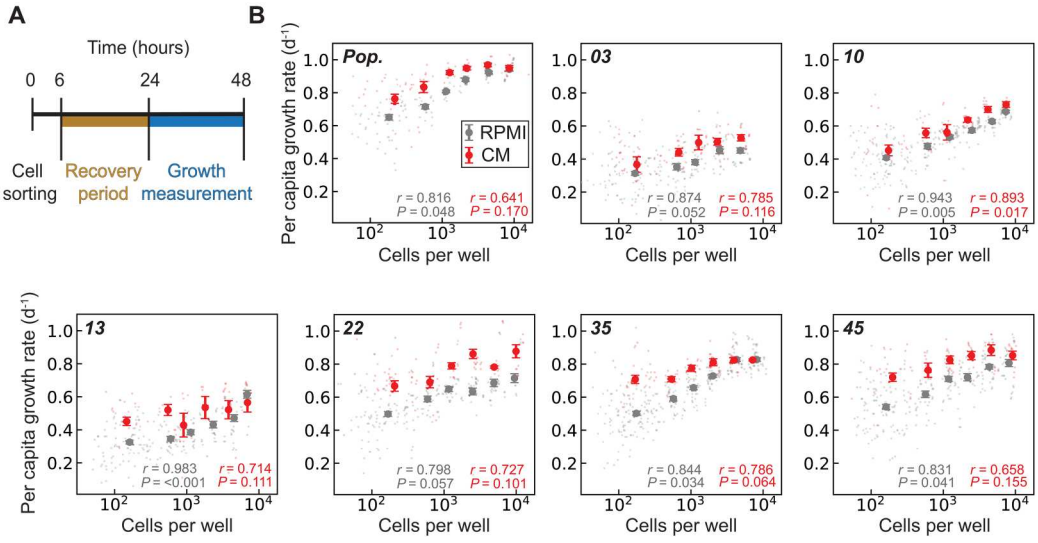

Fig. 2. The Allee effect, an ecological obstacle to clonal growth. (**A**) Scheme representing the experimental setup of the Operetta high-content imaging-based growth screen. (**B**) Plots of per capita growth rates across a range of cell densities from 63 to 49,866 cells/cm^2 in regular growth medium, RPMI (gray), or conditioned medium (CM) (red). Progressive binning of cell density was used to define each population: 0 to 1250 cells/cm^2 (bin 1), 1253 to 2500 cells/cm^2 (bin 2), 2503 to 5000 cells/cm^2 (bin 3), 5003 to 10,000 cells/cm^2 (bin 4), 10,003 to 20,000 cells/cm^2 (bin 5), and 20,003 to ∞ cells/cm^2 (bin 6). Data are represented as mean ± SEM. The correlation between binned growth rate and binned cell number in both RPMI and conditioned medium was evaluated for significance using Pearson's correlation conducted in R.

parental population as well as clones 10, 35, and 45, while clones 03, 13, and 22 were not significantly affected with P values of 0.224, 0.295, and 0.502, respectively (fig. S2A and data S6). Growth rates and mean migration speed displayed a significant anti-correlation (fig. S2B and data S5 and S6). Despite the relatively mild effect on migration speed, it is worth noting that even small differences in speed integrated for sufficiently long times can translate into meaningful differences in distance traveled. These data suggest that the phenotype switching at the heart of the go-or-grow dichotomy is influenced by cell density and can be modulated by soluble factors produced by the tumor community members.

Interclonal cross-feeding interactions underlie fitness improvement

The combined observations of population enhancement of clonal outgrowth and alleviation of the Allee effect in the presence of population-conditioned medium strongly suggested that there were functional interactions mediated by soluble factors between the lineages. This led us to ask whether specific ecological interactions could be identified within our collection of lineages. To address this question, we generated conditioned medium from each of the six independent lineages grown at 33,333 cells/cm^2. We then used the semi–high-throughput screen to perform cross-feeding experiments to evaluate the pairwise interaction landscape between individual lineages. Focusing on populations with densities of $N < 1250$ cells/cm^2, which were characterized by a stronger dependency on conditioned medium for maximal growth in our initial screen, we calculated the per capita growth rates for each of the cross-feeding conditions (Fig. 3A and data S7). The results revealed that although the vast majority (66.7%) of interactions were positive, 33.3% of interactions were neutral, with no significant benefit or detriment derived from the conditioned medium (Fig. 3A and data S7). These ratios shifted slightly in higher density cultures ($N > 1250$ cells/cm^2), with positive interactions still dominating the screen at 63.3%, and neutral interactions accounting for 30% (fig. S3A and data S7). Yet, in these conditions, we observed the emergence of some negative interactions, accounting for 6.7%. Although negative interactions were rare, notably, conditioned medium derived from clone 22 significantly repressed the growth of clone 45 at high ($N >$ 1250 cells/cm^2) cell densities (fig. S3A and data S7). Furthermore, in line with the Allee-like growth, we observed that clones 3, 10, 35, and 45 displayed self-feeding capable of boosting their own growth rates significantly, albeit for clones 3 and 45 only at low densities (Fig. 3B, fig. S3A, and data S7). Additionally, the screen also suggests the absence of a keystone population, in that no single lineage appears to be responsible for increasing the fitness across all populations. To validate the cross-feeding results in a coculture setting, we selected two strongly interacting lineages, 22 and 35, and set up an Operetta-based screen to assess the growth of clone 22 in RPMI or in coculture with clone 35. Clone 22 was seeded with the same range of densities as previously used: N ranging from 63 to 49,866 cells/cm^2 (fig. S3B and data S7). In the coculture setting, clone 35 was seeded with an initial seeding density of 1000 cells per well (3125 cells/cm$^{2)}$ or 2000 cells per well (6250 cells/cm^2) (fig. S3B and data S7). These densities were chosen based on their ability to enhance growth of clone 35 in a cell-autonomous setting (Fig. 2B). In this direct coculture setting, we observed a significant enhancement of growth for low-density cultures (<400 cells/cm^2) of clone 22 grown in the presence of clone 35 at both densities. Higher density cultures of clone 22 failed to show a significant growth enhancement, which was not unexpected given the Allee-type growth kinetics. Collectively, this screen revealed specific interlineage interactions that have the capacity to modulate growth at low cell densities, indicating a possible supportive role of small but phenotypically heterogeneous cellular communities, shared goods, and division of labor in the early establishment of tumors.

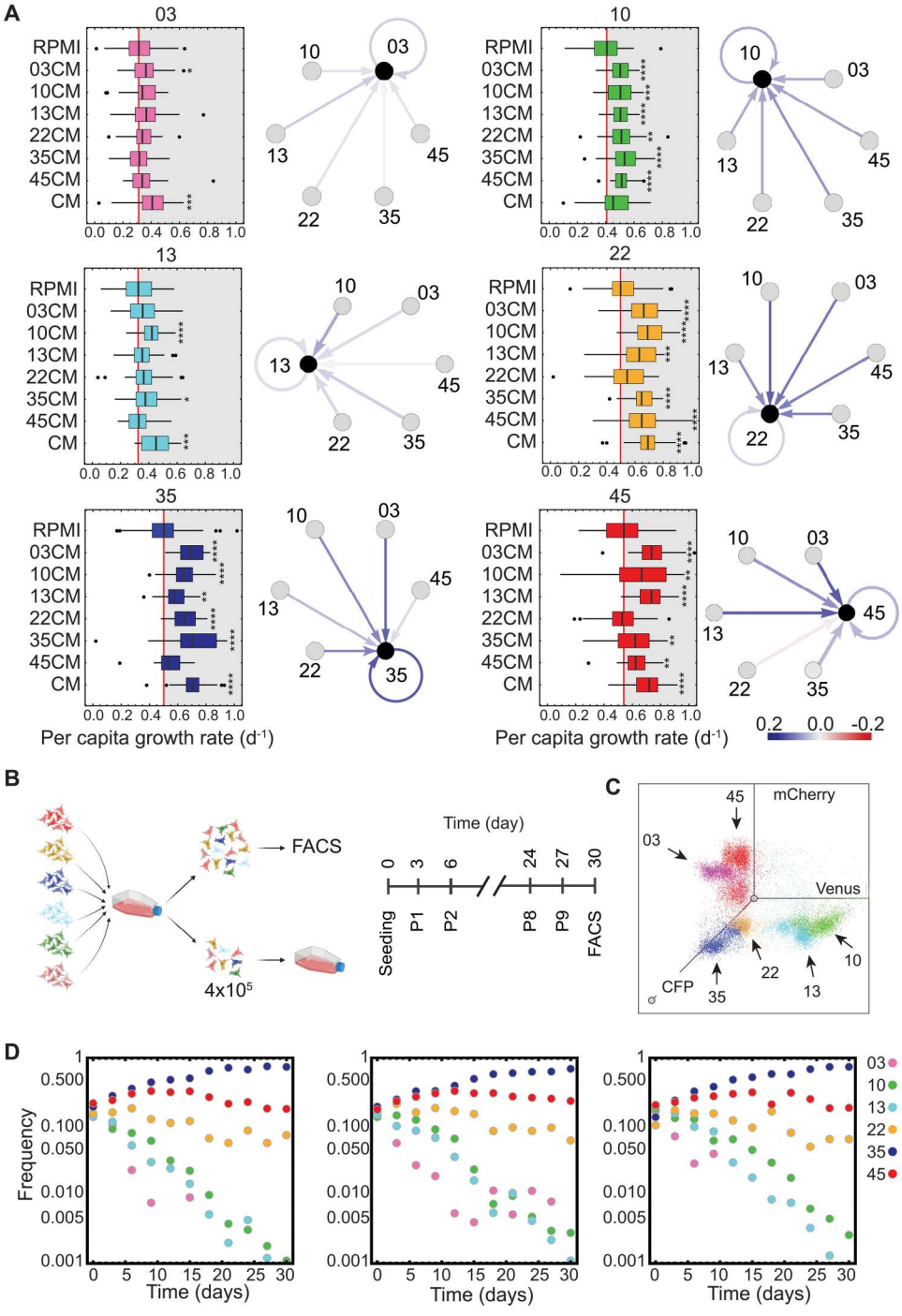

Fig. 3. Community interactions provide non–cell-autonomous alleviation of the Allee effect. (**A**) Box plots of the per capita growth rates of each lineage in RPMI, the six different lineage conditioned media, or conditioned medium. The data represented correspond to wells containing cells at a density of <1250 cells/cm^2. A one-way analysis of variance (ANOVA) was used to test for significant differences in growth rate for each lineage across the eight media. Post hoc unpaired *t* test was then conducted in R to identify significant differences between the growth rate of cells in RPMI, and each of the seven different conditioned media. *$P < 0.05$, **$P < 0.01$, ***$P < 0.001$, ****$P < 0.0001$. Network graphs reflect the relative strength of each cross-feeding interaction. Each node represents a lineage. Edges represent a cross-feeding interaction; the arrow indicates the direction of the cross-feeding. The color of the edge indicates the strength of the benefit confirmed by the interaction. (**B**) Left: Cartoon representation of a longitudinal coculture of the six distinct lineages. Right: Depiction of the experimental design. (**C**) A representative profile of the six-lineage combination culture at the time of seeding obtained using flow cytometry. (**D**) Graphical representation of the frequency of the six lineages over the course of three 30-day coculture experiments carried out in RPMI. Data were obtained by conducting a flow cytometry–based analysis of the leftover cells following each passage.

Ecological interactions stabilize intratumoral clonal diversity

Next, we wanted to test whether the interactions we observed using the Operetta growth screen were durable in the context of a long-term longitudinal coculture of all six isolated lineages. We seeded each one of our lineages as subpopulations in equal proportions in T25 flasks. The cells were then passaged through a bottleneck of 400,000 cells per vessel, every 3 days for 30 days (Fig. 3B). Then, the unique color profile of each lineage was used to quantify its frequency in the population by fluorescence-activated cell sorting (FACS) across the experimental window (Fig. 3C and fig. S4). This experiment was performed in both RPMI and parental population conditioned medium.

We first focused our attention on the culture maintained in RPMI and asked whether soluble factor exchange between the six lineages would alter their growth as a community. Tracking the lineages' proportions in the culture over time revealed the dominance of a stable "minimal interacting community" (MinIC) (*28*) composed of three lineages that evolved toward long-term coexistence with plateauing frequencies: 22, 35, and 45 (Fig. 3D; fig. S5, A and B; and data S8).

Conditioned medium enhanced fitness for all lineages when grown at low densities. Analysis of clonal behavior in conditioned medium revealed growth dynamics similar to those observed in RPMI for clones 03, 10, 13, and 22, suggesting that soluble factor exchange between the six clones was sufficient to recapitulate similar levels of shared goods found in the conditioned medium (fig. S5B). Clone 35 and 45 behaviors differed from those of the other four clones. Whereas their growth closely mirrored growth in RPMI during the first 10 days of the experiment, they later deviated significantly from their observed growth trajectories in the RPMI setting. This was frequency dependent, with a reduction in clone 45′s frequency occurring in conjunction with clone 35′s frequency surpassing 50%. The same trend was not observed in RPMI, despite similar clone 35 dominance, suggesting an interaction between the two clones specific to these conditions (fig. S5, A and B). Together, these data support a role for interlineage interactions in stabilizing diversity through modulation of individual fitness, as exemplified by the formation of the MinIC.

Clonal populations have distinct soluble metabolite profiles

Interclonal exchange of soluble proteins, such as growth factors, has previously been demonstrated to be a non–cell-autonomous driver of tumor growth (*13*, *29*). This prompted us to ask whether the observed fitness benefits bestowed by conditioned medium could be attributed to a protein component. First, we subjected both RPMI and parental culture–conditioned medium to a 3-kDa molecular weight cutoff filtration. This allowed for effective removal of all but the smallest molecular weight proteins and some peptides. Dilution cloning of the MDA-MB-231 cell line was then repeated using the protein-depleted RPMI and parental conditioned medium. The benefit conferred by conditioned medium was maintained (Fig. 4A and data S9). Through both cross-feeding and longitudinal coculture, we identified clone 22 as a component of the MinIC whose fitness is greatly enhanced by lineage-derived soluble factors. In an attempt to investigate the nature of the molecule(s) responsible for conferring this fitness benefit, we repeated the cross-feeding experiments as previously described using 3-kDa filtered RPMI and conditioned medium derived from the parental population, clones 35 and 45. Again, filtration did not ablate the enhancement of clone 22 growth rate conferred by the parental population, clone 35 or clone 45 conditioned medium (Fig. 4B and data S9). This suggested that the exchanged factor could be a small molecule or metabolite. It has previously been argued that the complex, spatially, and temporally varying structures and dynamics of microbial ecological systems are largely consequences of biological metabolism (*30*). Furthermore, work in microbial communities has demonstrated cooperative metabolite exchange to be a driver of community-level fitness (*31*, *32*). Single-sample gene set variation analysis (GSVA) on the Hallmark pathway collection for evaluating gene set enrichment using the transcriptomic profiles of the individual lineages suggested distinct metabolic differences between the three lineages (fig. S6A). An in-depth analysis using GSVA on selected Reactome metabolic pathways spanning from glycolysis to oxidative phosphorylation to lipid metabolic processes revealed significant variations in the gene set enrichment for these pathways between the three lineages (Fig. 4C). To address whether coculturing would alter these profiles, we performed a parallel transcriptomic analysis of the three lineages isolated from the longitudinal coculture. Samples were harvested following 15 days of coculture. Stark differences emerged in the GSVA analysis of both the entire collection of the Hallmark pathways and a subset of the Reactome metabolic pathways previously analyzed (fig. S6, B and C), suggesting that soluble factors released by the three lineages contribute to metabolic reprogramming upon coculture.

Therefore, we assessed the lineage's individual soluble metabolite profiles. Conditioned medium was harvested from each of the three interacting lineages and parental population cultures under growth conditions. Liquid tomography–mass spectrometry (LC-MS)–based semitargeted metabolic analysis was performed to assess lineage-specific metabolite consumption and production. These metabolite measurements revealed differences between the four populations (fig. S7 and data S10) that could not be accounted for by differences in growth rates, as exemplified by pyruvic acid, which, in line with the transcriptomic data, was more abundant in clone 22 conditioned medium with respect to clone 35′s conditioned medium, notwithstanding significant differences in the per capita growth rates between the two.

Motivated by the variations in gene set enrichment of lipid metabolic pathways between lineages that emerged from the GSVA, we decided to focus more specifically upon lipid metabolic pathways. Clustering performed on GSVA enrichment scores of Reactome Lipid and Fatty Acid pathways again revealed lineage-specific variations between the three study populations, with clone 35 clustering independently from clones 22 and 45 (Fig. 4D). Therefore, given the significant enhancement filtered clone 35 conditioned medium had on clone 22 growth together with the variation in gene set enhancement for lipid metabolism–associated pathways, we assessed the intra- and extracellular lipidomic and fatty acid profiles of clones 22 and 35 (fig. S8 and data S11). In line with the GSVA analysis of lipid metabolic pathways, both intra- and extracellular lipid profiles differed significantly between the two clones (Fig. 4E, fig. S8A, and data S11). Despite similar intracellular fatty acid profiles between the two clones, significant differences emerged in the analysis of the extracellular fatty acid profiles, with clone 22–derived medium showing an enrichment in fatty acid composition (Fig. 4F, fig. S8B, and data S11).

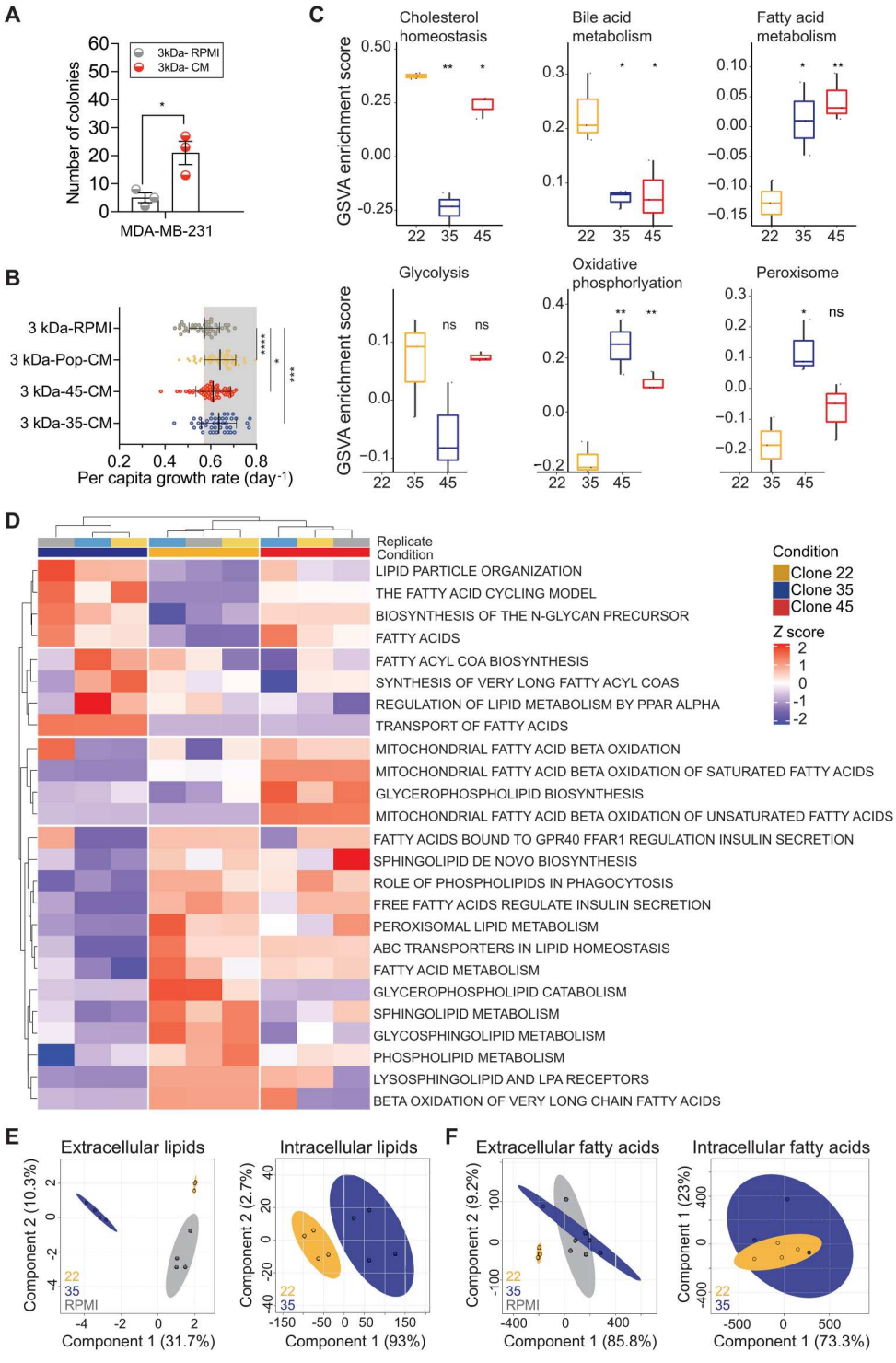

Fig. 4. Interlineage metabolic heterogeneity supports population fitness. (**A**) Single-cell colony formation assay conducted in 3-kDa filtered medium. Colony growth was assessed by microscopic evaluation of the plate 16 days after seeding. Clusters >10 cells were counted as a colony. Data are represented as mean ± SEM. Significance was determined in Prism 9 using a two-tailed Student's *t* test. (**B**) Growth of lineage 22 seeded at <1250 cells/cm^2 in 3-kDa filtered RPMI, conditioned medium, lineage 35 conditioned medium, or lineage 45 conditioned medium. Per capita growth rates were determined using the Operetta high-content imaging-based growth screen. (**C**) Box plots representing the distribution of gene set enrichment variation analysis (GSVA) scores for selected pathways. Data are represented as minimum, 25th percentile, median, 75th percentile, and maximum. Significance was determined using analysis of variance (ANOVA) followed by a two-tailed Student's *t* test. *P < 0.05, **P < 0.01, ***P < 0.001, ****P < 0.0001. (**D**) Heatmaps and single-sample unsupervised clustering showing the *z* scores of the GSVA enrichment scores for Reactome Lipid and Fatty Acid Metabolic pathways for transcriptomic data from lineage 22 (yellow), lineage 35 (blue), and lineage 45 (red). (**E**) Principal components analysis of extracellular (left) and intracellular (right) lipid species of lineage 35 (blue) and lineage 22 (yellow). (**F**) Principal components analysis of extracellular (left) and intracellular (right) fatty acid species of lineage 35 (blue) and lineage 22 (yellow).

To verify the heterogeneity of the lipid metabolic profiles, we asked whether the lineages would display a differential sensitivity to simvastatin. Statins are inhibitors of 3-hydroxy-3-methylglutaryl-coenzyme A reductase, an integral enzyme in the mevalonate pathway, which produces cholesterol along with a range of important intermediary metabolites including isoprenoid precursors, ubiquinone, dolichol, and isopentenyladenine (*33*). Consistent with previously published observations, simvastatin administration negatively affected the growth of all three lineages, with clone 35 displaying the highest sensitivity to the drug (fig. S8C) (*34*). Further evaluation of the density dependency to growth, calculated using the Pearson product-moment correlation coefficient for all three lineages, revealed that simvastatin treatment resulted in the loss of the previously observed relationship between fitness and seeding

density for clone 35 but not for clone 22 or 45 (Fig. 2B, fig. S8C, and data S12) Thus, despite being maintained in similar growth medium and culture conditions, there exists an extensive metabolic heterogeneity between the clones that is reflected in their soluble metabolomes. These results suggest the potential existence of a metabolic division of labor between tumor lineages. Models of metabolic division of labor have suggested it as a strategy to maximize community growth rate by streamlining of resources in other communities (*35*).

Clone-derived tumoroids display self-organization and multiclonal collective invasion

To test whether the community interactions in the MinIC provided a fitness advantage in a more physiologically relevant setting for cancer establishment, we decided to explore lineage and MinIC proliferative and invasive properties in a tumoroid setting. Briefly, either single lineages, at an initial density of 500 and 1500 cells, or the MinIC, seeded as a mixed population of 500 cells per lineage, were seeded into round-bottom plate in a 50% Matrigel:RPMI mixture and centrifuged to facilitate aggregation into a single tumoroid. Tumoroid growth and invasion were then monitored over a 6-day period. First, proliferation was measured using 5-ethynyl-2′-deoxyuridine incorporation (*24*). Analysis revealed a significant enhancement of proliferation in the MinIC-derived tumoroids when compared to tumoroids derived from single lineages (fig. S9, A and B, and data S13). Despite having been seeded as a well-mixed combination, over the course of 6 days of growth, the MinIC tumoroids reproducibly self-organized. The resultant tumoroids displayed a high degree of mixing between the three clones in the tumoroid interior and an enrichment of clone 35 at the periphery (Fig. 5A). Close inspection revealed that although clone 35 was enriched at the periphery, there was an extensive amount of mixing even at the periphery, with no apparent banding, a phenotype previously associated with strong mutualism (fig. S9C) (*36*, *37*). A similar mixing pattern emerged from clones seeded under geometrical confinement on micropatterned disks of 250 μm (fig. S9D). Visual inspection also revealed the presence of multicellular invasive protrusions emanating from the surface of the tumoroids, prompting an evaluation of their circularity. Although all tumoroids deviated from perfect circularity, clone 45 and MinIC-derived tumoroids deviated most significantly (Fig. 5B and data S13). Further evaluation of the invasive protrusions in the MinIC-derived tumoroids revealed that they were polyclonal in nature (Fig. 5C). This phenomenon of positive association between lineages in three-dimensional (3D) space is often observed in interacting communities. Since collective invasion is a precursor to metastatic dissemination, these findings prompted us to ask whether the tumors derived from the MinIC would have a higher metastatic burden.

Metastatic outgrowth is enhanced from polyclonal seedings derived from interacting lineages

Metastatic spread is a major cause of breast cancer–related deaths. There is now substantial evidence that polyclonal cell clusters have significantly higher propensity to seed metastases (*1*, *4*, *38*). In light of this, significant attention has been paid to elucidating the mechanisms of the polyclonal escape from the primary site with adhesion-driven collective migration from the primary site emerging as a major contributor (*4*, *39*, *40*). Yet, the question of why polyclonal seedings have enhanced metastatic capacity has not been sufficiently addressed. Our observations concerning the presence of an Allee-type growth kinetics and the alleviation of these effects by shared-metabolite ecological interactions (e.g., in conditioned medium) suggest a potential role for cooperative behavior among tumor cells at low cell densities with particular relevance to metastatic dissemination. MDA-MB-231 is a verified model for metastatic basal breast cancer, preferentially metastasizing to liver and lungs (*41*). Therefore, using our MDA-MB-231–derived lineages, we asked whether metastatic burden would be increased in mice with primary tumors seeded from MinIC of clones 22, 35, and 45 in comparison to mice seeded with tumors derived from a single lineage alone.

We performed orthotopic transplantation into the mammary fat pads of nonobese diabetic (NOD)–severe combined immunodeficient (SCID)-γ mice using the lineages alone or the MinIC and monitored tumor formation and metastatic dissemination to the liver and lungs (Fig. 5D and data S14). Tumors developed in all four conditions and had differing latencies consistent with their maximum per capita growth rates as determined in the Operetta screen (fig. S10, A and B). Mice were sacrificed at a predetermined tumor size of approximately 200 mm^3, and primary tumors, livers, and lungs were collected for analysis. Primary tumors from the MinIC cohort were analyzed for the lineage composition, by flow cytometry and confocal analysis. The lineages′ RGB colors were used together with an anti-human vimentin staining to identify specifically the MDA-MB-231 cells. Both analysis revealed that clone 45 was the predominate lineage, followed by clone 35 and then clone 22 (Fig. 5E; fig. S10, C and D; and data S14). Both hematoxylin and eosin staining and immunohistochemistry performed using anti-human vimentin antibody on sections from both lung and livers isolated from the tumor-bearing mice suggested that although all four lines were able to seed distal metastases, metastatic dissemination was more efficient in mice bearing tumors seeded from the MinIC (Fig. 5F and fig. S10, E and F). Taking advantage of the fluorescent barcoding together with immunofluorescence for human vimentin, confocal imaging of 100-μm sections was then performed to quantify metastatic dissemination and load. Analysis of these sections revealed that not only did the MinIC-derived tumors seed metastases more efficiently at both the lung and liver but also the resultant lung metastases were polyclonal in nature with a significantly higher metastatic load (Fig. 5, G and H; fig. S10F; and data S14). The observation of higher metastatic load in the MinIC seeded metastases supports the concept that community interactions are beneficial to overcoming barriers to growth in metastatic settings.

DISCUSSION

Despite the numerous "attempts" of establishment made over the course of our lifetimes, very few tumors will eventually progress to malignancies. It is attractive to hypothesize that this is due to the necessity for the tumors to develop cellular heterogeneity as well as stabilizing interactions to escape a growth barrier and establish malignancy. While there is now ample evidence that the tumor interacts with the local microenvironment (*42*, *43*), only a limited number of studies have addressed the contribution of intratumoral interactions to the tumor fitness landscape during tumor onset and metastatic dissemination (*1*, *13*, *38*). This is despite the high degree of lineage-specific phenotypic variability found in cancer and the

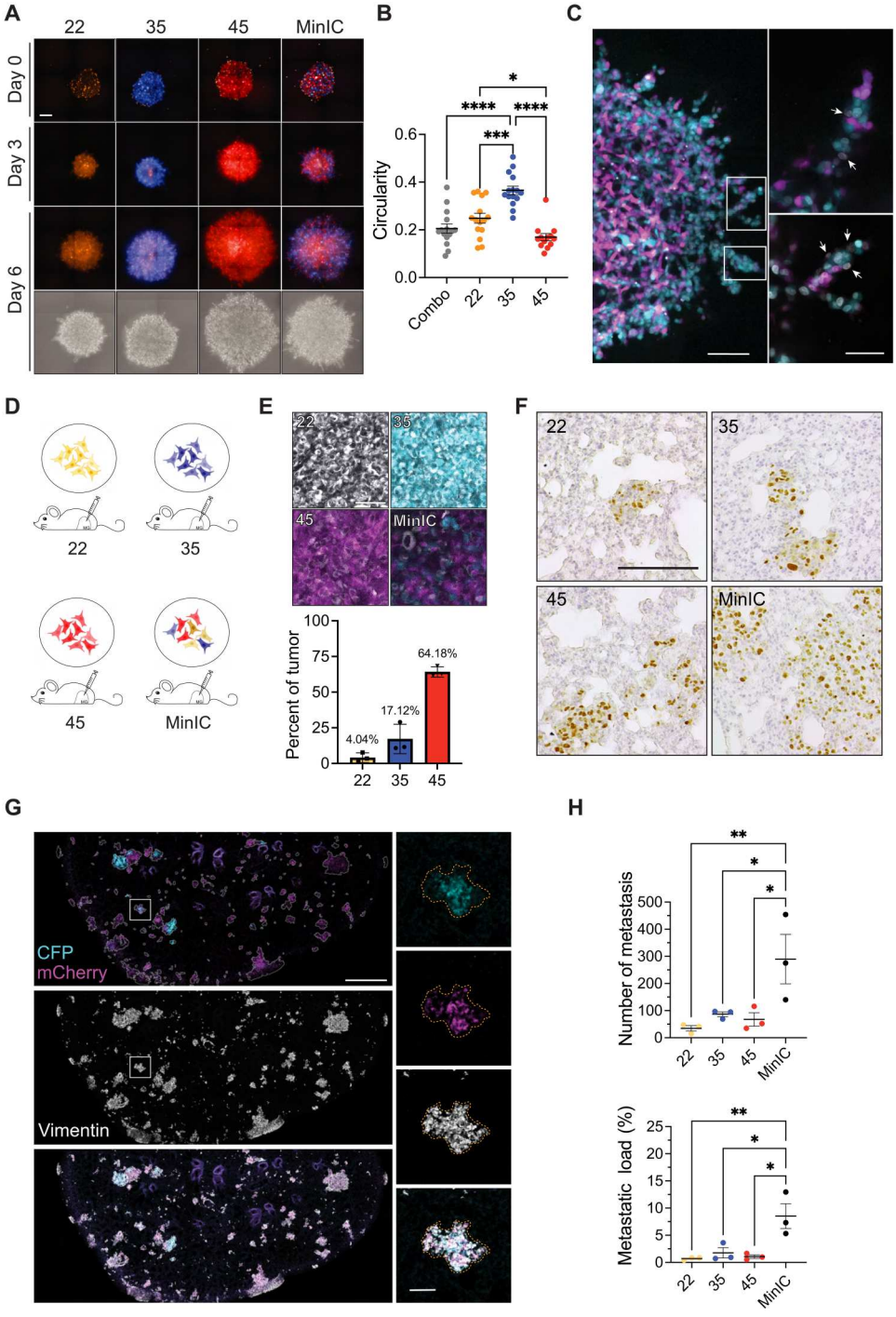

Fig. 5. Metastatic outgrowth is enhanced from minimal interacting community (MinIC)–derived polyclonal tumors. (**A**) Spheroids composed of lineage 22, lineage 35 (blue), lineage 45 (red), or the MinIC. Cells labeled with a nuclear dye (yellow). (Bottom) Spheroids after 6 days in culture. Scale bar, 100 μm. (**B**) Circularity of spheroids after 6 days in culture. Groups compared using an ordinary one-way analysis of variance (ANOVA) and then a Tukey's multiple comparisons test. (**C**) (Left) Confocal image of the center of a MinIC spheroid. Scale bar, 100 μm. (Right) Images of MinIC spheroid protrusions' lineage 35 (blue), lineage 45 (magenta), and all nuclei (gray). Lineage 22 is indicated with arrows. Scale bar, 50 μm. (**D**) The mammary fat pads of NOD-SCID mice were injected with 300,000 cells composed of lineage 22, lineage 35, lineage 45, or a combination of the three. (**E**) Confocal images of primary tumors. Scale bar, 50 μm. (Left) Contribution of each lineage to MinIC primary tumor determined by imaging fixed tumor cross-sections. Anti-human vimentin antibody facilitated tumor cell detection (gray). (Right) The endogenous fluorescence of lineage 35 (blue) and lineage 45 (magenta) was used to quantify their contributions. (**F**) Immunohistochemical staining of human nuclei in mouse lung metastases. Scale bar, 100 μm. (**G**) Confocal image of lung tissue from a mouse harboring a MinIC tumor. Cancer cells were identified with an anti-human vimentin antibody (white). The endogenous fluorescence of lineages 35 (blue) and lineage 45 (magenta) was used to identify them. Scale bars, 1000 μm (top left) and 100 μm (bottom right). (**H**) Quantification metastasis (top) and metastatic load (bottom) in lungs of mice from each study group. Anti-human vimentin antibody was used to identify metastases. An ordinary one-way ANOVA, followed by a Fisher's least significant difference (LSD) test. $^{*}P < 0.05$, $^{**}P < 0.01$, $^{***}P < 0.001$, $^{****}P < 0.0001$. Data are represented as mean ± SEM. Statistical tests were conducted using Prism 9.

association between high intratumoral heterogeneity and poor patient outcomes in a variety of clinical settings (*44*–*46*). A more thorough mechanistic understanding of how clonal diversity contributes to disease progression will ultimately enable the development of more effective therapeutic strategies.

Here, we demonstrated that ecological interactions exist between phenotypically diverse lineages isolated from tumor cell lines. The mechanism and consequences of this interaction provide important insights into the role of interlineage interactions in metastatic progression. First, we provide evidence that these interactions are mediated, at least in part, by soluble metabolite exchange. Although metabolite exchange has been shown to be a common driver of microbial community assembly (*32*), functional metabolite exchange among distinct tumor lineages remains a relatively unexplored aspect of intratumor heterogeneity. Our data suggest that the cooperation occurs through multiple metabolic shared goods, and not through a single metabolite. Tumor microenvironmental factors have been shown to lead to the development of metabolic

diversification driven by difference in oxygen and nutrient availability (*47*). Yet, the metabolic diversity found between the lineages used in this study was found between cell populations grown in rich medium under identical culture conditions. This suggests the existence of a division of labor, as defined by functional complementarity or synergistic advantage, among tumor lineages.

Second, we demonstrated that this diversification was functional by showing that this interlineage soluble factor exchange was necessary and sufficient to alleviate Allee barriers to growth both in vitro and in vivo in metastatic settings. Although the presence and the extent of Allee effects in tumor settings remain largely unstudied, there is emerging evidence from preclinical and clinical studies that it plays a relevant role even in the context of a tissue (*24*, *48*, *49*). Here, we investigated the lineage variation in Allee barriers through the establishment of a semi–high-throughput imaging screen. This strategy allowed us to measure per capita growth rates across a wider range of cell seeding densities than would not have been possible with conventional cell growth assays. For lineages grown in RPMI, this screen revealed a significant correlation between density and growth. The strength of this correlation varied between lineages, suggesting a potential range in weak Allee strength and hence in lineages' ability to proliferate at low densities. Despite the variations in Allee strength across the cohort, exposure to conditioned medium weakened the observed correlation between density and growth for all lineages. This suggests that lineage cooperation, through soluble factor exchange, is able to alleviate Allee barriers to growth.

Tumor growth models predominately assume exponential growth kinetics even at low densities, largely ignoring the potential role of the Allee effect in tumor settings. Allee effect is most relevant at low densities such as those found during tumor initiation and metastatic dissemination. Therefore, to address whether cooperation between distinct lineages was able to overcome the barriers to growth imposed by a weak Allee effect in vivo, we performed orthotopic injection of the MinIC, or its single constituents. We then assessed the resulting primary tumors as well as metastatic dissemination to lungs and livers. In line with the role of ecological interactions in fueling growth at low densities, we found enhanced metastatic outgrowth in mice injected with the MinIC. Although single lineages were able to seed metastasis, our data suggested that the resultant metastases lacked the proliferative potential of the polyclonal MinIC-derived metastases. Metabolic adaptation may be a requirement for cancer progression, as each step in the metastatic cascade presents a metabolically distinct environment from that of the primary site (*50*–*52*). Several reports have focused on elucidating the mechanisms by which metastatic tumor cells adapt their metabolism. We find that the MinIC interacted through soluble metabolite exchange and that this exchange is sufficient to improve growth rates of the community members. Therefore, it is attractive to hypothesize that polyclonal metastases modulate community fitness through transport of a metabolic ecological niche, thereby facilitating metastatic outgrowth in organs with nutrient profiles different from their tissue of origin. Such a mechanism would allow the population to retain proliferative potential while adapting their metabolism to the new environment. Although this requires further validation, through targeted modulation of metabolic networks within the community, these findings provide a potential explanation for why polyclonal metastases are more efficient in fueling metastatic outgrowth. Yet, they also imply that monoclonal metastases, or external forces that reduce the polyclonality of the metastases, could negatively affect the proliferative potential of the disseminated tumor cells, potentially pushing them into dormancy; the implications of which are discussed below.

In breast cancer, tumor reoccurrence is the leading cause of breast cancer–related death. These reoccurrences are often at distal sites and can emerge up to 20 years following the initial therapeutic intervention (*53*). It is largely believed that these reoccurrences are fueled by dormant populations that reawakened by as yet unknown mechanisms (*54*). Despite the technical limitations in capturing growth kinetics of very small populations in clinical or preclinical settings, the hypothesis that Allee effect growth kinetics play a role into this scenario could provide valuable mechanistic insight. Recent work characterizing the clonal composition of matched primary and metastatic samples from a large cohort of breast, colorectal, and lung cancer patients found that polyclonal seedings were common in untreated lymph and distal metastasis (*55*). However, clonal composition was significantly reduced following adjuvant therapy. Our study suggests that therapy-driven alterations in clonal diversity could eliminate a functional community, thereby making the persisting clones vulnerable to a weak Allee effect, which at low densities would be accompanied by long lag times, potentially creating a pool of dormant cells. Future studies focusing on ecological regulation of therapy-induced dormancy in reawakening may provide additional insight and confirmation of this possibility.

MATERIALS AND METHODS

Cell culture

The BT474 (Leibniz Institute DSMZ—German Collection of Microorganisms), MDA-MB-231 (American Type Culture Collection), and MCF7 (National Cancer Institute) cell lines were cultured in RPMI 1640 (Lonza, BE12-167F or Euroclone, ECB9006L) supplemented with 10% dialyzed FBS (Euroclone, ECS0181L) and 2 mM L-glutamine (Euroclone, LOBE17605F). The hTERT RPE-1 (American Type Culture Collection) cells were cultured in Dulbecco's minimum essential medium (DMEM)/F12 and GlutaMAX (Life Technologies, 31331-098) supplemented with 10% dialyzed FBS and 1 mM sodium pyruvate (Microtech, L0642). All cells were cultured at 37°C, 5% CO_2. Cells were passaged when they reached approximately 60 to 80% confluence unless otherwise specified. Cells were harvested using trypsin-EDTA (Euroclone, ECB3052D-20), pelleted by centrifugation at 1200 rpm for 5 min, and reseeded as needed.

Karyotyping

Approximately 8×10^5 cells were seeded into T25 flasks 1 day before use. Cell culture medium was supplemented with colcemid solution (Gibco, 15212-012). The MDA-MB-231, MCF7, and RPE-1 cell lines were treated with colcemid (0.1 μg/ml) for 3 hours at 37°C, 5% CO_2. The BT474 cell line was treated with 0.05 μg overnight at 37°C, 5% CO_2. Following treatment, both the cell culture medium and the cells were harvested and centrifuged at 1200 rpm for 5 min. Following centrifugation, the medium was removed and 5 ml of 37°C hypotonic solution (5.6 g of KCl in 1 liter of H_2O) was added dropwise. The suspension was incubated at 37°C for 30 min. Next, three drops of ice-cold Carnoy fixative (3:1 methanol:

acetic acid solution) was added. Cells were then pelleted at 1200 rpm for 5 min. Supernatant was removed, and the remaining cells were resuspended in 5 ml of ice-cold Carnoy fixative and incubated at 4°C for 30 min. This process was repeated one additional time. Following the second round of fixation, cells were resuspended in approximately 300 μl of Carnoy fixative and dropped onto a slide wetted with 4°C deionized water. Slides were allowed to dry before being stained with Giemsa stain (Sigma-Aldrich, GS500). After staining, slides were washed with MilliQ H_20 and allowed to dry overnight. Metaphases were acquired with an RGB camera (Nikon Digital Sight, DS-5MC) mounted on an Olympus Upright BX51 Full Manual widefield microscope. Chromosomes were counted using ImageJ software.

Conditioned medium and control medium

Conditioned medium for MDA-MB-231, MCF7, and BT474 cell lines was made by seeding cells at 1×10^5cells/ml and 33,333 cells/cm^2 in regular growth medium in cell culture flasks. RPE-1 conditioned medium was produced by seeding 0.5×10^5 cells/ml and 16,666 cells/cm^2. After seeding, cells were allowed to grow for approximately 24 hours at 37°C, 5% CO_2. The conditioned medium was then collected and passed through a 0.22-μm filter. Following filtration, the conditioned medium was stored in single-use aliquots at −20°C until use. Control medium was produced in the same manner, without the addition of cells. Immediately before use, the control and conditioned media were thawed and supplemented with 30% regular growth medium and 1% penicillin streptomycin (Euroclone, ECB3001L). Unless otherwise specified in the text, this mixture is referred to as "conditioned medium."

Dilution cloning

Cell lines were harvested at approximately 70% confluence. Trypsin was inactivated using culture medium, and then the cells were centrifuged at 1200 rpm for 5 min. Following centrifugation, cells were resuspended in an appropriate volume of culture medium, passed through a 45-μm filter, and counted using a Berker chamber. Cells were then serially diluted until approximately 50 cells were present in 10 ml of medium. The medium (100 μl per well) was then dispensed across a 96-well tissue culture plate (Corning, 3596). Forty-eight hours after seeding, an additional 100 μl of medium was added to each well. Thereafter, the medium was changed every 48 hours for the duration of the experiment, 16 days for the MDA-MB-231, MCF7, and BT474 cell lines and approximately 8 days for the RPE-1 cell line. On the last day of the experiment, wells with at least 10 cells were counted as colonies for the MDA-MB-231, MCF7, and RPE-1 cells. Wells with at least five cells were counted as containing a colony for the BT474 cell line. On the final day of the experiment, images were taken of colonies using Evos FL (Life Technologies). Colony sizes were determined using ImageJ software. For the MCF7, BT474, and RPE-1 cell lines, colony borders were traced and the area of the colonies was reported. For the MDA-MB-231 individual cells, or for very large colonies, a subset of individual cells was counted and used to approximate colony size.

Generation of barcoded MDA-MB-231 clone cohort

The MDA-MB-231, MCF7, and BT474 cell lines were barcoded using a previously published lentivirus-based system (*17*, *18*). The three lentivirus constructs used to barcode the cell lines were produced with LeGO-V2 Venus (Addgene, 27340), LeGO-C2 mCherry (Addgene, 27339), and LeGO-Cre2 Cerulean (Addgene, 27338). LeGO vectors were all gifts from B. Fehse and were deposited in Addgene. The following packaging plasmids were used to assemble to lentivirus constructs in human embryonic kidney (HEK) 293T cells (Interlab Cell Line Collection): pRSV-Rev (Addgene, 12253), pMDLg/pRRE (Addgene, 12251), and pMD2.G (Addgene, 12259). Each viral construct was titrated in all of the target cell lines. One multiplicity of infection of each viral construct was used to barcode the cell lines. After barcoding, the cell lines were maintained for several weeks in culture. Following this period, the MDA-MB-231 and MCF7 cell lines were dilution-cloned. In brief, cells were seeded in 96-well plate (Costar, 3596) wells containing 100 μl of conditioned medium. The cells were seeded at a concentration of 0.5 cells per well. MDA-MB-231 lineages were expanded to 24-well plate, at which point they were harvested, frozen back, and stored in liquid nitrogen until use. While in culture, the MDA-MB-231 lineages were maintained in their parental population's conditioned medium. The lineages' medium was changed approximately every 48 to 72 hours.

Clone morphological classification

Cells were seeded at approximately 1×10^5 cells per well in 24-well plate wells containing a glass coverslip coated with fibronectin from human plasma (20 μg/ml) (Sigma-Aldrich, F1056-5MG) diluted in Dulbecco's phosphate-buffered saline (DPBS). Before imaging, cells were fixed with 4% formaldehyde solution (Sigma-Aldrich, 1.00496.8350) for 10 min and then mounted for imaging in glycerol. Approximately 400 cells per clone were imaged using a TCS SP5 confocal microscope (Leica) mounted with a 63× oil objective. The barcoded fluorescence signatures composed of cyan fluorescent protein (CFP) excitation/emission maxima λ 433/475 nm, yellow fluorescent protein (YFP) excitation/emission maxima λ 513/530 nm, and/or mCherry excitation/emission maxima λ 587/610 nm of the lineages were used to identify their morphological features. Clone 22's morphology was characterized based on a phalloidin-TRITC (tetramethyl rhodamine isothiocyanate), excitation/emission maxima λ 540/565 nm, staining because it did not have an endogenous fluorescence signature. In brief, fixed clone 22 cells were permeabilized with 0.01% Triton X-100 (BioChemica, EMR237500) in 1× PBS. The cells were then stained with phalloidin-TRITC (Sigma-Aldrich, P1951), diluted at 1:100 in a 3% bovine serum albumin (BSA) and 1× PBS solution for 1 hour at room temperature. Finally, the cells were washed three times for 10 min in 1× PBS. The nuclei of all lineages were stained with DAPI (Sigma-Aldrich, D9542), diluted 1:5000 in 1× PBS for 15 min at room temperature followed by three 10-min washes in 1× PBS. Coverslips were mounted in a 70% glycerol (Carlo ERBA, 453752), 30% 1× PBS, 1.5% DABCO (Sigma-Aldrich, D2522) solution and imaged.

CellProfiler was used to extract the metrics that informed the classifications of the lineages by morphology. To cluster lineages based on their morphological parameters, the cell shape was extracted with a custom Fiji (*56*) plugin and CellProfiler pipeline (*57*). The Fiji plugin extracts the maximum projection of the DAPI and the sum projection of the maximum projection of the other three channels. This sum projection is then filtered with a median filter, masked using the MinError[3] threshold method, and then Gaussian-filtered. The CellProfiler pipeline identifies the nuclei using the IdentifyPrimaryObject with two class parameters after Otsu's

threshold method on the maximum projection of the nuclei channel. Then, the cell boundaries are recognized using the IdentifySecondaryObject with propagation method on the sum projection retrieved by the Fiji script, using the nuclei identified as primary object. The morphological parameters measured were averaged, normalized, and then used by the Seaborn clustermap python function to extract the dendrogram.

Nucleic acid extraction and RNA sequencing

Clonal populations were seeded in six-well plate wells (Corning, 353056) at 2×10^5 cells per well in 1.5 ml of RPMI 1640, supplemented with 2 mM L-glutamine and 10% dialyzed FBS. After approximately 24 hours at 37°C, 5% CO_2, the culture medium was removed and the monolayer was washed once with 1× DPBS. After removal of the DPBS, 800 μl of TRIzol (Life Technologies, 15596026) was added directly to the cells. The cells were detached into the TRIzol by scrapping and then frozen at −80°C until processing. In brief, RNA was phase-separated by adding 200 μl of chloroform (Sigma-Aldrich, 372978-100ml), followed by centrifugation and collection of the entire aqueous phase. The RNA was then precipitated using 0.5 ml of isopropanol and pelleted by centrifugation. The pellet was washed with 75% ethanol/water solution before being dried and resuspended in ribonuclease (RNase)–free water. Following the extraction, RNA was processed using the RNeasy Mini Kit (Qiagen, 74104) including the optional treatment with RNase-Free DNase (Qiagen, 79254). RNA quality was checked using Agilent Bioanalyzer 2100. Samples were then processed and analyzed by the IFOM-Cogentech facility. The Stranded mRNA Preparation Ligation Kit (Illumina) was used for library preparation, starting from 500 ng of RNA. Libraries were quality-checked using a Qubit HS DNA kit before sequencing. Paired-end sequencing (2 × 75 nucleotides) was performed using NextSeq550Dx (Illumina). An average of 40 million pair end reads were generated per library. Read alignment and quality check were performed with the nf-core rnaseq pipeline (*58*). In particular, reads were aligned to the GRCh38/hg38 assembly human reference genome using the STAR aligner (v 2.6.1d) (*59*) and quantified using Salmon (*v1.4.0*) (*60*). Differential gene expression analysis was performed using the Bioconductor package DESeq2 (v1.30.0) (*61*). Single-sample GSVA for evaluating pathway enrichment in transcriptional data was carried out using the Bioconductor package GSVA (v1.38.2) (*62*) on the Hallmark and Reactome gene sets available from MSigDB (https://www.gsea-msigdb.org/gsea/msigdb/genesets.jsp?collections). GSVA was performed starting from variance-stabilizing transformed expression values by modeling RNA-sequencing (RNA-seq) data by a Poisson distribution and calculating the score using a Kolmogorov-Smirnov random walk statistic. *Z* score for clustered heatmaps was calculated with the Bioconductor pheatmap package using the scale_rows function.

Operetta growth screen

Immediately before seeding, cells were harvested using trypsin-EDTA, pelleted by centrifugation at 1200 rpm for 5 min, and resuspended in 1% dialyzed FBS, 1× DPBS. Cells were then seeded at a range of cell densities from 93 to 20,000 cells per cm^2, as prescribed by a randomized plate layout, in Cell Carrier Ultra 96-well plate wells (PerkinElmer, 6055302) containing 100 μl of the medium of interest supplemented with 1% penicillin-streptomycin. Cells were seeded with a BD FACSAria Ilu. SiR-DNA (200 nM) (excitation/emission maxima λ 652/674 nm; SPIROCHROME, SC007) was added to medium for nuclear identification. After the cells had adhered to the plate, an Operetta CLS imaging system equipped with a 20×/1.0 NA (numerical aperture) water objective was used to image each well in both bright-field and Alexa Fluor 647, maintaining the correct temperature and CO_2 concentration. Images were acquired on days 0, 1, and 2 after seeding. The measured change in cell number between days 1 and 2 was used to calculate the doubling times, and per capita growth rates were reported. Nuclei recognition and counting were done using Harmony software version 4.9.

Coculture lineage 22 and lineage 35

Cocultures of lineages 22 and 35 were conducted using the previously described Operetta growth screen. At days 1 and 2 of the screen, each plate was acquired with the Operetta CLS, in widefield mode, binning 2 × 2, equipped with a 20×/1.0 NA water immersion objective and the following filters: Alexa Fluor 405 excitation/emission maxima λ 420/500 and Alexa Fluor 647 excitation/emission maxima λ 645/760. Nuclei recognition and counting were done using Harmony software version 4.9. A gray value threshold of 12,000 was used to identify lineage 35, which contains an endogenous CFP fluorescent protein.

Free range migration assay

MDA-MB-231 cells, both clones and parental population, were seeded at approximately 3150 cells per cm^2 in 24-well tissue culture plates (Corning Costar, 3526). Twenty-four hours after seeding, the culture medium was changed. The new culture medium was spiked with 500 nM SiR-DNA. Ten fields of view per well were imaged, every 5 min, for approximately 10 hours. Time-lapse movies were recorded using a ScanR system (Olympus) equipped with an IX81 inverted microscope provided with an ORCA-AG camera (Hamamatsu), using a 10×/0.3 NA objective. The system is driven by the Olympus CellCens Dimension software 1.18 (build 16686). Temperature and CO_2 concentration were controlled for the duration of the experiment using an OKOlab incubator. Nuclei tracking was done using ImageJ. Trajectory analysis was performed in R.

Design and setup of six-way coculture experiment

Each of the six MDA-MB-231 lineages was harvested using trypsin, and 0.67×10^5 cells per lineage were seeded into combination cultures, a six-well plate well, or a seeding control for fixation with 1% paraformaldehyde (PFA) and flow cytometry analysis. Every 3 days thereafter, cells were harvested using trypsin, counted, and reseeded at 4×10^5 cells/T25 flask in 8 ml of culture medium. The control lineages were maintained in isolation in six-well plate wells and passaged at 1:2 and 1:5 split ratios as needed. Following each passage, leftover cells were pelleted, resuspended in 1× DPBS, and fixed with a 1% formaldehyde solution for 25 min at 4°C. The cells were then pelleted at 1200 rpm for 5 min at 4°C and washed once in 1× DPBS solution. Following the wash, the cells were stored in 1× DPBS at 4°C until FACS analysis. Samples were acquired with Attune Nxt (Life Technologies). The following lasers were used for excitation of the sample: 405 nm, 488 nm, and 561 nm. Analysis of FACS data was done using Kaluza Analysis Software (Beckman Coulter Life Sciences). The coculture experiment was conducted in both

conditioned medium and RPMI 1640 supplemented with 2 mM L-glutamine and 10% dialyzed FBS.

Micropatterning of the MinIC

Micropatterns of 250-μm-dimeter circles were produced using photolithography. In brief, glass coverslips were activated with a plasma cleaner before coating with Poly(L-Lysine)-PEG methyl ether (PLL-PEG) solution (0.2 mg/ml) diluted in 10 mM Hepes solution. After washing with MilliQ water, the cell-refractory PLL-Peg coating was removed in the circular regions by passing deep ultraviolet (UV) light through a chromium photomask. Following the selective removal of the PLL-Peg coating form the circular patterns, the exposed glass was coated with fibronectin (10 μg/ml) in 1× PBS. After coating with fibronectin for approximately 3 hours at 37°C, the coverslips were washed three times with 1× PBS. The three lineages comprising the MinIC were then harvested using trypsin. Each lineage was counted and seeded onto the coverslips at approximately 10,416 cells/cm^2. After cell adhesion, the medium was changed and replaced with fresh culture medium. Cells were maintained in culture for 24 to 48 hours before fixation with 4% PFA and mounting on glass coverslips in a 70% glycerol, 30% 1× PBS, 1.5% DABCO solution. Images of the MinIC seeded on patterns were acquired using an SP5 inverted confocal microscope equipped with a 63× oil objective.

MDA-MB-231 spheroid generation

Clones 22, 35, and 45 were seeded into ultra-low cluster, 96-well, round-bottom, ultra-low attachment polystyrene plates (Costar, 7007) and kept on ice for the duration of the seeding protocol. Lineages were seeded alone at 500 or 1500 cells per well or in a combination culture composed of 500 cells from clones 22, 35, and 45. Before seeding, cell suspension was incubated with IncuCyte NucLight Rapid Red Reagent (ESSEN Bioscience, 4717) to facilitate nuclear identification. The IncuCyte NucLight Rapid Red Reagent was used at a 1:1000 dilution in regular growth medium at room temperature in the dark for approximately 30 min. Upon seeding, the plates were centrifuged at 1200 rpm for 5 min at 4°C. The medium was then removed from each well, leaving 15 μl of medium in each well. Then, 40 μl of ice-cold, 50% 3-D reduced growth factor basement membrane extract (RGF BME) (Cultrex, 3445-005-001), 50% regular growth medium was added dropwise to the center of each well, being careful to avoid introducing bubbles. Plates were then centrifuged at 1200 rpm for 5 min at 4°C. Following the second centrifugation, the cell aggregates were imaged with an Evos FL microscope equipped with a 20× objective and then incubated at 37°C, 5% CO_2 for approximately 20 min. Finally, 100 μl of regular growth medium was added to each well. At 6 hours, 3 days, and 6 days after seeding, images of the spheroids were acquired using the Operetta CLS system, in widefield nonconfocal mode, binning 2 × 2, equipped with a 20×/0.4 NA air objective and the following filters: Alexa Fluor 405 CFP excitation/emission maxima λ 420/500, mCherry excitation/emission maxima λ 560/650, and Alexa Fluor 647 excitation/emission maxima λ 645/760. The 3D structures of the spheroids were acquired using 15-μm step sizes. The maximum projections of the bright-field images of spheroids acquired 6 days after seeding were analyzed with a custom Fiji macro, in which the images of the spheroids were segmented in binary images and then assessed for circularity.

EdU incorporation for MDA-MB-231 spheroids

Following 6 days in culture, spheroids were incubated with 10 μM 5′-ethynyl-2′-deoxyuridine (*24*) (Invitrogen, E10187) in regular culture medium for approximately 2.5 hours at 37°C, 5% CO_2. The medium was then removed, and the spheroids were fixed with 200 μl per well of 4% formaldehyde solution overnight at 4°C. Following fixation, spheroids were washed three times with 200 μl per well with 3% BSA (Seqens, 1005-70), 1× DPBS. Spheroids were then permeabilized with 0.5% Triton X-100 (Euroclone, EMR237500) in 1× DPBS for 20 min at room temperature. Next, spheroids were washed twice with 3% BSA in 1× DPBS, 200 μl per well, being careful to remove all wash solution from each well following the second wash. Spheroids were then incubated at room temperature for approximately 1 hour in, 100 μl per well, Click-iT reaction cocktail prepared per the manufacturer′s instructions. Click-iT reaction cocktail contained Click-iT Reaction Buffer (Invitrogen, C10641B), $CuSO_4$ (Invitrogen, C10641C), EdU Buffer Additive (Invitrogen, C10641E), and Alexa Fluor 350 picolyl azide (Invitrogen, C10645B). Following incubation, the reaction cocktail was removed and the spheroids were washed three times with 200 μl per well of 1× DPBS. Spheroids were stored at 4°C, protected from light until mounting and imaging.

Spheroids were mounted and imaged as follows. A square opening was cut out of a piece of 500-μm-thick Press to Seal Silicone Sheet (Invitrogen, P18178). The cut spacer was then pressed onto a glass coverslip. Spheroids were removed from 96-well plate wells using a transfer pipette (VWR, 612-4486) and placed into the opening in the center of the silicon spacer. PBS (1×) was removed from the coverslips. The spheroids were then washed once with approximately 60 μl of Omnipaque 350 (GE Healthcare, V08AB03). An additional 60 μl of Omnipaque 350 was used to submerge the spheroids on the coverslip. The spheroids were then overlaid with a glass coverslip, which was attached to the glass slide with a bead of silicon. The mounted spheroids were kept at room temperature and imaged within 3 days of mounting. Imaging of the spheroids was done using a TCS SP8-DLS confocal microscope (Leica) equipped with a 25× water objective and a 20× air objective.

Quantification of EdU incorporation in MDA-MB-231 spheroids

The quantification of spheroid cellularity was performed with Arivis Vision4D version 3.1.4 using a customized pipeline. In brief, images were denoised via a median filter (radius 2) and then segmented via the blob finder tool (diameter 10 mm, threshold 4%, split sensitivity 80) on the nuclear channel. All the segmented objects that had a volume between 100 and 5000 μm^3 as well as a *y* axis bounding box shorter than 500 pixels were considered as cell nuclei. From these total nuclei, the EdU intensity associated with each nucleus was assessed. Nuclei with a mean EdU signal intensity greater than 20 were considered as proliferating nuclei. The percentage of identified nuclei that were also EdU positive were reported for each spheroid. More than 2000 nuclei were sampled for each spheroid.

Orthotopic injection

Four groups of three female NOD-SCID mice, approximately 2 months of age, were injected with 300,000 cells per site in mammary fat pad 4L. The cells injected were clone 22, 35, 45, or a combination (*28*) composed of an equal proportion of the three.

Before injection, cells were suspended in 1× DPBS, 5% Matrigel (Cultrex, 3445-005-01), and 0.1% trypan blue (Sigma-Aldrich, T8150-100ML). The cells were injected into the mammary fat pad in 50 μl of suspension medium. Following injection, mice were periodically monitored, and when possible, the tumors were measured using calipers. Mice were euthanized by asphyxiation with CO_2 when the tumor reached a volume of approximately 200 mm^3. Upon euthanasia, the primary tumor was removed and weighed before processing. Mice were perfused with 10 ml of ice-cold MilliQ-H20 containing heparin (10 U/ml) (Sigma-Aldrich, H3149) and 0.45% NaCl before collection of primary tumor, lungs, and liver. All animal experiments were approved by the OPBA (Organisms for the well-being of the animal) of IFOM and Cogentech. All experiments complied with national guidelines and legislation for animal experimentation. All mice were bred and maintained under specific pathogen–free conditions in our animal facilities at Cogentech Consortium at the FIRC Institute of Molecular Oncology Foundation and at the European Institute of Oncology in Milan, under the authorization from the Italian Ministry of Health (Autorizzazione N° 604-2016).

Tissue preparation for imaging

Lung, liver, and one-half of each tumor section were fixed in 4% formaldehyde (VWR BDH Chemicals, 9713.1000) for approximately 16 hours at 4°C, followed by a wash in 1× PBS for 24 hours at 4°C. Fixed samples were then embedded in 3% low–melting point agarose (Euroclone, EMR911100). Sections (100 μm) were cut using a vibratome (Leica S1200). Sections were suspended in blocking solution composed of 5% BSA and 0.3% Triton X-100 (Euroclone, EMR237500) in 1× PBS and incubated for 1 hour at room temperature. After blocking, tissues were stained with anti-human α-vimentin (Vector Laboratories, VP-RM17), diluted 1:100 in blocking solution, overnight at 4°C. Tissues were then washed for at least three 2-hour washes at 4°C. Tissues were then incubated overnight at 4°C with the secondary antibody donkey anti-rabbit Alexa Fluor 647 (Thermo Fisher Scientific, A31573) diluted at 1:400 in blocking solution. Tissues were washed three more times for at least 2 hours per wash in 1× DPBS. A postfixation for 5 min in 4% formaldehyde solution was then performed. Following postfixation, tissues were washed three times in 1× PBS before staining for 10 min at room temperature with DAPI diluted 1:5000 in 1× PBS. Three washes in 1× PBS were them performed, and the sections were mounted on slides (VWR, 631-1560) in curing mounting medium (Thermo Fisher Scientific, P36961). Sections were acquired using a confocal microscope (Leica TCS SP8-DLS) equipped with a 10×/0.3 NA objective. Image analysis was done using a custom Fiji plugin built by the IFOM Imaging unit described below.

Metastasis quantification from immunofluorescence

A custom Fiji plugin was used to extract vimentin-, CFP-, and mCherry-positive areas. Before vimentin channel segmentation, Fiji's manually adjusted Li thresholding method was applied. To enhance object detection, the segmented image was subjected to an erosion-dilation process followed by a Gaussian blur filter (sigma 5 pixels) and then segmented again with the Fiji default method. A metastasis was defined as a vimentin-positive area greater than 500 μm^2. Fiji's analyze particles plugin was used to determine the total metastatic area. Before segmentation of the CFP and mCherry channels, the subtract background tool with a rolling ball radius of 200 pixels and a Gaussian filter, sigma radius 1 pixel, were both applied. For segmentation, the manually adjusted MaxEntropy ImageJ thresholding method was used. After segmentation, the despeckle filter was used to remove small unspecific particles. These regions of interest (ROIs) were then used to assess the fraction of vimentin-positive area that was also positive for either CFP or mCherry.

Immunohistochemistry

Fixed lungs, livers, and tumors were processed using a Diapath automatic processor. In brief, tissues were dehydrated through exposure to 70% ethanol for 60 min, two 90-min washes in 95% ethanol, and three 60-min washes in 99% ethanol. Tissues were then cleared through three 90-min washes in xylene. Finally, the tissues were subjected to three 1-hour immersions in paraffin. Paraffin-embedded samples were stored at room temperature until cutting. Hematoxylin and eosin staining (Diapath) was performed on serial sections to assess histological features. For immunohistochemistry, paraffin was removed with xylene and sections were rehydrated in graded alcohol. Antigen retrieval was carried out using preheated target retrieval solution for 30 min. Endogenous peroxidase activity was quenched with 3% hydrogen peroxide in distilled water for 10 min at room temperature. The tissue sections were blocked with FBS in 1× PBS for 60 min and then incubated overnight with primary antibody, anti-human nuclei diluted 1:200 (Millipore, MAB4383 clone 3E1.3). The primary antibody was detected using a polymer detection kit (Microtech, GAM-HRP) followed by a diaminobenzidine chromogen reaction (Vector Laboratories, Peroxidase substrate kit, DAB, SK-4100). All sections were stained with Mayer's hematoxylin and visualized using a bright-field microscope.

Flow cytometry analysis of primary tumors

Upon euthanasia, primary tumors were excised. The tumors were cut in half lengthwise, one-half for fixation as described previously, and the other half was placed in ice-cold 1× PBS. The tumors were then transferred to a 10-cm petri dish and minced with a sterile scalpel. The minced tumors were transferred into a 15-ml falcon tube containing and enzyme digestion medium containing DMEM, 1% glutamine, 1% penicillin streptomycin, collagenase from *Clostridium histolyticum* (Merck, C2674-500MG) at 200 U/ml, and hyaluronidase from bovine testes (Merck, H4272-30MG) at 10 mg/ml. Minced tumors were incubated in the digestions medium at 37°C, 5% CO_2 for 3 hours. Following digestion, the tumor cell aggregates were broken up by pipetting. The tumor digests were then centrifuged at 600 rpm for 5 min, and the resulting pellets were then resuspended in 1 ml of trypsin and incubated for 5 min at 37°C, 5% CO_2. Trypsin was then inactivated with 10 ml of RPMI 1640 supplemented with 10% FBS. Cells were then passed through first a 100-μm filter (Falcon, 352360) and then a 40-μm filter (Falcon, 352340). Next, the cells were centrifuged at 1400 rpm for 5 min. Pelleted cells were resuspended in 1 ml of Red Blood Cell Lysing Buffer Hybri-Max (Merck, R7757) and incubated at room temperature for 1 min. Following the incubation, 9 ml of 1× DPBS was added. Cells were then pelleted, washed once with 1× PBS, and resuspended in 1 ml of 1× PBS. Cells were counted and adjusted to approximately 1×10^6 cells/ml in 1× PBS. LIVE/DEAD Fixable Yellow Dead Cell Stain (1 μl/ml) (Thermo Fisher Scientific, L34967), reconstituted in 50 μl of dimethyl sulfoxide

(DMSO), was added. The cells were incubated with the LIVE/DEAD Fixable Yellow Dead Cell Stain for 30 min on ice in the dark. Cells were washed once with 1 ml of 1× PBS and fixed in 1% formaldehyde solution in PBS on ice for 30 min. After fixation, cells were washed twice with 1 ml of 1× PBS containing 1% FBS and 1% BSA. After washing, cells were resuspended in 2 ml of blocking buffer composed of 10% BSA in 1× PBS and incubated for 30 min at 4°C in the dark. After blocking, cells were centrifuged at 1200 rpm, 4°C for 5 min and the blocking solution was removed. Cells were then resuspended in 200 μl of CD44 antibody, anti-human, phycoerythrin (PE) (Miltenyi Biotec, 130-113-335) diluted 1:100 in 1% BSA in 1× PBS, and incubated on ice, in the dark, for 45 min. Cells were then spun at 1200 rpm, 4°C for 5 min, and the antibody solution was removed. The cells were then washed twice with 1 ml of 1× PBS, 5% BSA before being resuspended in 1× PBS. Cells were stored at 4°C in 1× PBS in the dark until FACS analysis. Acquisition of samples was performed with Attune NxT (Thermo Fisher Scientific). mCherry and PE signals were acquired using the YL2 (620/15) and YL1 (585/16) channels on the yellow laser, respectively. The CFP signal was acquired using the VL1 channel (440/50) on the violet laser.

The 3-kDa filtration

Centricon Plus-70 (Merck Millipore Ltd., UFC700308) was used to filter conditioned medium and control medium generated as previously described. Before use, filters were prerinsed with sterile MilliQ H_2O. Approximately 50 ml of sterile water was loaded into the filter. The filter was spun at 3000 relative centrifugal force (rfc) for 15 min, water was removed, and the column was subjected to a reverse spin at 1500 rfc for 5 min to remove any residual water from the column. Next, columns were loaded with a maximum of 70 ml of medium and spun for 60 min at 4°C, 3000 rfc. Following filtration, the medium was passed through a 0.22-μm filter and stored in single-use aliquots at −20°C. Immediately before use, the filtered control and conditioned media were thawed and supplemented with 30% regular growth medium and 1% penicillin-streptomycin.

Metabolomics

Clones 22, 35, and 45 were seeded in 25 ml of medium in T75 flasks at 33,333 cells/cm^2 in RPMI at 37°C, 5% CO_2. After 24 hours in culture, 100 μl of conditioned medium was harvested from the flask, passed through a 0.22-μm filter, and snap-frozen with dry ice in an ultra-low cluster, 96-well round-bottom ultra-low attachment polystyrene plate. Samples were stored at −80°C until processing. Medium supernatant samples were extracted by adding 30 μl of defrosted sample to 10 μl of internal standard (100 μM glutamine 13C5 in water), followed by 100 μl of ice-cold 1:1 acetonitrile (ACN):water. Samples were incubated at 4°C for 30 min and centrifuged at 3200*g* at 4°C for 10 min, and 40 μl of the supernatant was transferred to a fresh polymerase chain reaction (PCR) plate, sealed with a pierceable sealing film for analysis. On an Agilent 1290 Infinity II UPLC system, 1 μl of sample was injected on the Waters Atlantis Premier BEH Z-HILIC Column (1.7 μm, 2.1 mm × 100 mm), maintained at 35°C, using a flow of 0.3 ml/min and an initial buffer composition of 20% buffer A [15 mM ammonium bicarbonate in water (Fisher, Optima grade), adjusted to pH 9 with ammonium hydroxide] and 80% buffer B [15 mM ammonium bicarbonate in 9:1 ACN:water (Fisher, Optima grade), adjusted to pH 9 with ammonium hydroxide], remaining constant for 3 min, ramping to 45% B over 4 min, remaining constant for 1 min, then returning to initial conditions. The total run time was 10 min. The LC was coupled to an Agilent 6470 triple quadrupole mass spectrometer, operating in dynamic multiple reaction monitoring (MRM) mode. Parameters for the Agilent JetStream ESI source were as follows: gas temperature: 200°C, gas flow: 13 liters/min, nebulizer: 60 psi, sheath gas temperature: 300°C, sheath gas flow: 11 liters/min, capillary (positive): 3500 V, capillary (negative): 2500 V, nozzle voltage (positive): 1000 V, nozzle voltage (negative): 500 V. The cycle time was Cycle 1000 ms. Data were analyzed using MassHunter Workstation Quantitative Analysis for QQQ v10.1. Compounds were identified based on retention time and fragmentation patterns matching to analytical standards. External calibration over eight serial dilution levels was used to convert peak areas to concentrations. The area of the internal standard (relative to the median area across all samples) was then used for further normalization. Data analysis and visualization were done using RStudio version 1.2.1093.

Lipidomics

Distinct lineages of MDA-MB-231 cells were seeded in six-well tissue culture plates at 1×10^6 cells per well in 2 ml of RPMI. The medium alone (2 ml) was placed in an additional well to serve as a medium control. Cells and control medium were maintained in culture overnight at 37°C, 5% CO_2. At the time of sample collection, the medium was taken from each well, snap-frozen on dry ice, and stored at −80°C for eventual processing and analysis of the extracellular lipid profile. For the assessment of intracellular lipidomes, cells were harvested via trypsinization. Culture medium was used to inactivate the trypsin. The cell pellet was washed twice with 1× DPBS before being resuspended in 200 μl of cold MilliQ H2O. Lipids were extracted and processed using a single-step extraction protocol with methanol and chloroform as described previously (*63*). In brief, cells were lysed by passing them repeatedly through a 26-gauge needle. Samples were then stored at −20°C until processing. Processing: 20 μl of sample was added to 5 μl of 5× lysis buffer containing 10% NP-40 and 2% SDS in 1× PBS. Following a 30-min incubation on ice, the samples were centrifuged at 13,000*g* for 20 min at 4°C. The clarified lysates were quantified using the Bradford assay. An equivalent of 50 μg of protein per sample was then used for the lipid extraction. In brief, the resuspended pellets were supplemented with cold water to obtain a final volume of 170 μl per sample, and then 700 μl of methanol was added. Samples were sonicated using Bioruptor for 60 s at 4°C. Cold chloroform (350 μl) was added. Samples were vortexed and incubated on an orbital shaker for 15 min at 4°C. In total, 350 μl of a 1:1 chloroform:water mixture was then added to each sample. Next, samples were vortexed and centrifuged at 13,000*g* for 10 min at 4°C. The lower phase was carefully isolated and desiccated in a SpeedVac before being resuspended in 50 μl of a buffer composed of 95% mobile phase A (ACN:H_2O 40:60; 5 mM NH_4COOCH_3; 0.1% HCOOH) and 5% mobile phase B (Isopropyl alcohol:H_2O 90:10; 5 mM NH_4COOCH_3; 0.1% HCOOH).

Medium samples were thawed. Then, to remove proteins, 400 μl from each sample was filtered through a 3-kDa cutoff micron filter (Millipore) by centrifugation for 20 min at 13,000*g*. Filtered medium was divided in two aliquots; 170 μl of each aliquot was spiked with 0.5 μl of SPLASH LIPIDOMIX Mass Spec Standard. Lipid extraction was performed by adding 700 μl of methanol to

each sample, followed by sonication for 1 min at 4°C. Next, 350 μl of chloroform was added to each sample. Samples were mixed on an orbital shaker for 15 min at 4°C. Then, 350 μl of water/chloroform (1:1, v/v) was added to each sample. The samples were then centrifuged at 13,000*g* for 10 min at 4°C. The lower phase of each sample was carefully isolated and desiccated in a SpeedVac before being resuspended and pooled with the appropriate paired aliquot in 25 μl of a buffer composed of 10% of ethanol and 90% of buffer made of 95% mobile phase A (ACN:H_2O 40:60; 5 mM NH_4COOCH_3; 0.1% HCOOH) and 5% mobile phase B (IPA:H_2O 90:10; 5 mM NH_4COOCH_3; 0.1% HCOOH).

Next, 1 μl of extracted lipids was diluted 1:5 and injected on the liquid chromatography system nLC Ekspert nanoLC400 set in nanoconfiguration coupled with Triple TOF 6600. Chromatography was performed using an in-house packed nanocolumn Kinetex EVO C18, 1.7 μm, 100 A (Phenomenex, Torrance, CA, USA), 0.75 × 100 mm at room temperature. The gradient started at 5% mobile phase B and was linearly increased to 100% B in 5 min, maintained for 45 min, then returned to the initial ratio in 2 min, and maintained for 8 min at a flow rate of 150 nl/min. The samples were analyzed in technical duplicate, in positive mode with electrospray ionization. Data acquisition and processing were performed with Analyst TF (version 1.7.1, AB SCIEX, Foster City, CA, USA). The following parameters were used: CUR 10 psi, GAS1 0 psi, GAS2 0 psi, source temperature 80°C, capillary voltage 2000 V. Spectra were acquired by full-mass scan from 200 to 1700 mass/charge ratio (m/z) and information-dependent acquisition (IDA) from 50 to 1800 m/z (top 8 spectra per cycle). The declustering potential was fixed at 80 eV, and the collision energy was fixed at 40 eV; target ions were excluded for 20 s after two occurrences. Wiff files were processed using the open-source software MS-DIAL version 4.60. The parameters were as follows: MS1 tolerance = 0.01 Da, MS/MS tolerance = 0.025 Da, MS1 mass range = 100 to 1700 Da, and minimum peak height = 10,000 amplitude. All other parameters were kept at the default values. Lipids were annotated using the MS-DIAL internal lipid database. Only the lipids showing MS/MS spectral similarity to the reference spectra in the MS-DIAL internal database and eluting at the predicted retention times were used for the analysis. The peak areas of annotated lipids were normalized by sum and statistically analyzed using the freely available online software metaboanalyst (https://www.metaboanalyst.ca/).

Simvastatin treatment

Simvastatin (MedChemExpress, HY17502) was resuspended at 20 mM in DMSO and stored in single-use aliquots at −80°C. Cell growth upon simvastatin treatment was assessed using the aforementioned Operetta growth screen. Cells were seeded as previously described into wells containing RPMI supplemented with 0.01% DMSO or simvastatin at a concentration 0.5, 1, or 2 μM.

Data analysis

Reads were aligned to the GRCh38/hg38 assembly human reference genome using the STAR aligner (v 2.6.1d) (*59*) and quantified using Salmon (v1.4.0) (*60*). Differential gene expression analysis was performed using the Bioconductor package DESeq2 (v1.30.0) (*61*), which estimates variance-mean dependence in count data from high-throughput sequencing data and tests for differential expression exploiting a negative binomial distribution-based model. Principal components analysis was performed with the plotPCA function in DeSeq2 package, which takes into account the top 500 most variable genes, that is, the genes that show the highest variability across samples, selected by highest row variance.

Null model of growth for the six-way coculture experiment

To investigate in quantitative terms the interdependences of the lineages in the six-way coculture experiment, we developed a simple mathematical model of growth that predicts the dynamics of the intrapopulation frequencies of the lineages over time under the assumption of independent growth.

The experiment consists in cycles of free growth (3 days), followed by random sampling and reseeding at lower density and counting. We modeled this experimental setup as a series of cycles of exponential growth, described by the following equation of motion

$$\begin{cases} \frac{d\,x_i(t)}{dt} = [r_i(c) - \langle r(t)\rangle]x_i(t) \\ \langle r(t)\rangle = \sum_{i=1}^{6} r_i(c)x_i(t) \end{cases} \quad (1)$$

where $x_i(t)$ is the intrapopulation frequency of lineage i at a given point in time t, and $r_i(c)$ is its expected growth rate of the ith clone, during the cycle c. We solved Eq. 1 for each cycle separately and required the initial condition to equal the end point of the previous cycle. In the first cycle, the initial condition was set to equal the initial frequencies of cells seeded at the beginning of the experiment.

Growth rates of the lineages were modeled as follows. First, to impose independence between lineages, the growth rate of each lineage is assumed to not depend on the frequency of the other coexisting lineages. Second, to account for the observed Allee effects, the growth rate $[r_i(c)]$ is assumed to be a function of the number $N_i(t_c^0)$, i.e., the number of cells of lineage i present in the well at the beginning of the cth cycle (at time t_c^0). The dependence of the growth rate on the number of cells is the one observed in Fig. 2B.

Statistical analysis

Statistical analyses were conducted using Prism 9 version 9.4.0, RStudio version 1.3.1093, or Python 3.8 as specified in the figure legends. P values less than or equal to 0.05 were considered significant, unless otherwise indicated in instances when corrections for multiple testing were applied. P values are denoted throughout the text as follows: (>0.05, ns), (<0.05, *), (<0.01, **), (<0.001, ***), (<0.0001, ****).

Supplementary Materials

This PDF file includes:
Figs. S1 to S10
Legends for Data S1 to S14

Other Supplementary Material for this manuscript includes the following:
Data S1 to S14

REFERENCES AND NOTES

1. M. Janiszewska, D. P. Tabassum, Z. Castaño, S. Cristea, K. N. Yamamoto, N. L. Kingston, K. C. Murphy, S. Shu, N. W. Harper, C. G. Del Alcazar, M. Alečković, M. B. Ekram, O. Cohen, M. Kwak, Y. Qin, T. Laszewski, A. Luoma, A. Marusyk, K. W. Wucherpfennig, N. Wagle, R. Fan,

F. Michor, S. S. McAllister, K. Polyak, Subclonal cooperation drives metastasis by modulating local and systemic immune microenvironments. *Nat. Cell Biol.* **21**, 879–888 (2019).
2. A. Marusyk, V. Almendro, K. Polyak, Intra-tumour heterogeneity: A looking glass for cancer? *Nat. Rev. Cancer* **12**, 323–334 (2012).
3. M. Karaayvaz, S. Cristea, S. M. Gillespie, A. P. Patel, R. Mylvaganam, C. C. Luo, M. C. Specht, B. E. Bernstein, F. Michor, L. W. Ellisen, Unravelling subclonal heterogeneity and aggressive disease states in TNBC through single-cell RNA-seq. *Nat. Commun.* **9**, 3588 (2018).
4. K. J. Cheung, V. Padmanaban, V. Silvestri, K. Schipper, J. D. Cohen, A. N. Fairchild, M. A. Gorin, J. E. Verdone, K. J. Pienta, J. S. Bader, A. J. Ewald, Polyclonal breast cancer metastases arise from collective dissemination of keratin 14-expressing tumor cell clusters. *Proc. Natl. Acad. Sci. U.S.A.* **113**, E854–E863 (2016).
5. A. Sharma, E. Merritt, X. Hu, A. Cruz, C. Jiang, H. Sarkodie, Z. Zhou, J. Malhotra, G. M. Riedlinger, S. De, Non-genetic intra-tumor heterogeneity is a major predictor of phenotypic heterogeneity and ongoing evolutionary dynamics in lung tumors. *Cell Rep.* **29**, 2164–2174.e5 (2019).
6. D. C. Minussi, M. D. Nicholson, H. Ye, A. Davis, K. Wang, T. Baker, M. Tarabichi, E. Sei, H. Du, M. Rabbani, C. Peng, M. Hu, S. Bai, Y. W. Lin, A. Schalck, A. Multani, J. Ma, T. O. McDonald, A. Casasent, A. Barrera, H. Chen, B. Lim, B. Arun, F. Meric-Bernstam, P. Van Loo, F. Michor, N. E. Navin, Breast tumours maintain a reservoir of subclonal diversity during expansion. *Nature* **592**, 302–308 (2021).
7. G. D'Souza, S. Shitut, D. Preussger, G. Yousif, S. Waschina, C. Kost, Ecology and evolution of metabolic cross-feeding interactions in bacteria. *Nat. Prod. Rep.* **35**, 455–488 (2018).
8. B. H. Good, M. J. McDonald, J. E. Barrick, R. E. Lenski, M. M. Desai, The dynamics of molecular evolution over 60,000 generations. *Nature* **551**, 45–50 (2017).
9. T. Bertero, W. M. Oldham, E. M. Grasset, I. Bourget, E. Boulter, S. Pisano, P. Hofman, F. Bellvert, G. Meneguzzi, D. V. Bulavin, S. Estrach, C. C. Feral, S. Y. Chan, A. Bozec, C. Gaggioli, Tumor-stroma mechanics coordinate amino acid availability to sustain tumor growth and malignancy. *Cell Metab.* **29**, 124–140.e10 (2019).
10. C. M. Sousa, D. E. Biancur, X. Wang, C. J. Halbrook, M. H. Sherman, L. Zhang, D. Kremer, R. F. Hwang, A. K. Witkiewicz, H. Ying, J. M. Asara, R. M. Evans, L. C. Cantley, C. A. Lyssiotis, A. C. Kimmelman, Pancreatic stellate cells support tumour metabolism through autophagic alanine secretion. *Nature* **536**, 479–483 (2016).
11. M. Archetti, D. A. Ferraro, G. Christofori, Heterogeneity for IGF-II production maintained by public goods dynamics in neuroendocrine pancreatic cancer. *Proc. Natl. Acad. Sci. U.S.A.* **112**, 1833–1838 (2015).
12. P. Martinez, N. J. Birkbak, M. Gerlinger, N. McGranahan, R. A. Burrell, A. J. Rowan, T. Joshi, R. Fisher, J. Larkin, Z. Szallasi, C. Swanton, Parallel evolution of tumour subclones mimics diversity between tumours. *J. Pathol.* **230**, 356–364 (2013).
13. A. Marusyk, D. P. Tabassum, P. M. Altrock, V. Almendro, F. Michor, K. Polyak, Non-cell-autonomous driving of tumour growth supports sub-clonal heterogeneity. *Nature* **514**, 54–58 (2014).
14. W. C. Allee, *Animal Aaggregations: A Study in General Sociology* (The University of Chicago Press, 1931).
15. F. Courchamp, T. Clutton-Brock, B. Grenfell, Inverse density dependence and the Allee effect. *Trends Ecol. Evol.* **14**, 405–410 (1999).
16. R. L. Milne, B. Burwinkel, K. Michailidou, J.-I. Arias-Perez, M. P. Zamora, P. Menendez-Rodriguez, D. Hardisson, M. Mendiola, A. Gonzalez-Neira, G. Pita, M. R. Alonso, J. Dennis, Q. Wang, M. K. Bolla, A. Swerdlow, A. Ashworth, N. Orr, M. Schoemaker, Y.-D. Ko, H. Brauch, U. Hamann; GENICA Network, I. L. Andrulis, J. A. Knight, G. Glendon, S. Tchatchou; kConFab Investigators; Australian Ovarian Cancer Study Group, K. Matsuo, H. Ito, H. Iwata, K. Tajima, J. Li, J. S. Brand, H. Brenner, A. K. Dieffenbach, V. Arndt, C. Stegmaier, D. Lambrechts, G. Peuteman, M.-R. Christiaens, A. Smeets, A. Jakubowska, J. Lubinski, K. Jaworska-Bieniek, K. Durda, M. Hartman, M. Hui, W. Y. Lim, C. W. Chan, F. Marme, R. Yang, P. Bugert, A. Lindblom, S. Margolin, M. Garcia-Closas, S. J. Chanock, J. Lissowska, J. D. Figueroa, S. E. Bojesen, B. G. Nordestgaard, H. Flyger, M. J. Hooning, M. Kriege, A. M. W. van den Ouweland, L. B. Koppert, O. Fletcher, N. Johnson, I. dos-Santos-Silva, J. Peto, W. Zheng, S. Deming-Halverson, M. J. Shrubsole, J. Long, J. Chang-Claude, A. Rudolph, P. Seibold, D. Flesch-Janys, R. Winqvist, K. Pylkas, A. Jukkola-Vuorinen, M. Grip, A. Cox, S. S. Cross, M. W. R. Reed, M. K. Schmidt, A. Broeks, S. Cornelissen, L. Braaf, D. Kang, J.-Y. Choi, S. K. Park, D.-Y. Noh, J. Simard, M. Dumont, M. S. Goldberg, F. Labreche, P. A. Fasching, A. Hein, A. B. Ekici, M. W. Beckmann, P. Radice, P. Peterlongo, J. Azzollini, M. Barile, E. Sawyer, I. Tomlinson, M. Kerin, N. Miller, J. L. Hopper, D. F. Schmidt, E. Makalic, M. C. Southey, S. H. Teo, C. H. Yip, K. Sivanandan, W.-T. Tay, C.-Y. Shen, C.-N. Hsiung, J.-C. Yu, M.-F. Hou, P. Guenel, T. Truong, M. Sanchez, C. Mulot, W. Blot, Q. Cai, H. Nevanlinna, T. A. Muranen, K. Aittomaki, C. Blomqvist, A. H. Wu, C.-C. Tseng, D. Van Den Berg, D. O. Stram, N. Bogdanova, T. Dork, K. Muir, A. Lophatananon, S. Stewart-Brown, P. Siriwanarangsan, A. Mannermaa, V. Kataja, V.-M. Kosma, J. M. Hartikainen, X.-O. Shu, W. Lu, Y.-T. Gao, B. Zhang, F. J. Couch, A. E. Toland; TNBCC, D. Yannoukakos, S. Sangrajrang, J. McKay, X. Wang, J. E. Olson, C. Vachon, K. Purrington, G. Severi, L. Baglietto, C. A. Haiman, B. E. Henderson, F. Schumacher, L. Le Marchand, P. Devilee, R. A. E. M. Tollenaar, C. Seynaeve, K. Czene, M. Eriksson, K. Humphreys, H. Darabi, S. Ahmed, M. Shah, P. D. P. Pharoah, P. Hall, G. G. Giles, J. Benitez, A. M. Dunning, G. Chenevix-Trench, D. F. Easton, Common non-synonymous SNPs associated with breast cancer susceptibility: Findings from the Breast Cancer Association Consortium. *Hum. Mol. Genet.* **23**, 6096–6111 (2014).
17. K. Weber, M. Thomaschewski, M. Warlich, T. Volz, K. Cornils, B. Niebuhr, M. Tager, M. Lutgehetmann, J. M. Pollok, C. Stocking, M. Dandri, D. Benten, B. Fehse, RGB marking facilitates multicolor clonal cell tracking. *Nat. Med.* **17**, 504–509 (2011).
18. K. Weber, M. Thomaschewski, D. Benten, B. Fehse, RGB marking with lentiviral vectors for multicolor clonal cell tracking. *Nat. Protoc.* **7**, 839–849 (2012).
19. P.-H. Wu, D. M. Gilkes, J. M. Phillip, A. Narkar, T. W.-T. Cheng, J. Marchand, M.-H. Lee, R. Li, D. Wirtz, Single-cell morphology encodes metastatic potential. *Sci. Adv.* **6**, eaaw6938 (2020).
20. D. R. Stirling, A. E. Carpenter, B. A. Cimini, CellProfiler Analyst 3.0: Accessible data exploration and machine learning for image analysis. *Bioinformatics* **37**, 3992–3994 (2021).
21. N. T. Fadai, M. J. Simpson, Population dynamics with threshold effects give rise to a diverse family of Allee effects. *Bull. Math. Biol.* **82**, 74 (2020).
22. F. Courchamp, L. Berec, J. Gascoigne, *Allee Effects in Ecology and Conservation* (Oxford Univ. Press, 2008).
23. P. Amarasekare, Spatial dynamics of mutualistic interactions. *J. Anim. Ecol.* **73**, 128–142 (2004).
24. Z. Neufeld, W. von Witt, D. Lakatos, J. Wang, B. Hegedus, A. Czirok, The role of Allee effect in modelling post resection recurrence of glioblastoma. *PLOS Comput. Biol.* **13**, e1005818 (2017).
25. K. E. Johnson, G. Howard, W. Mo, M. K. Strasser, E. A. B. F. Lima, S. Huang, A. Brock, Cancer cell population growth kinetics at low densities deviate from the exponential growth model and suggest an Allee effect. *PLOS Biol.* **17**, e3000399 (2019).
26. K. Bottger, H. Hatzikirou, A. Voss-Bohme, E. A. Cavalcanti-Adam, M. A. Herrero, A. Deutsch, An emerging Allee effect is critical for tumor initiation and persistence. *PLOS Comput. Biol.* **11**, e1004366 (2015).
27. I. Hecht, S. Natan, A. Zaritsky, H. Levine, I. Tsarfaty, E. Ben-Jacob, The motility-proliferation-metabolism interplay during metastatic invasion. *Sci. Rep.* **5**, 13538 (2015).
28. L. R. Yates, M. Gerstung, S. Knappskog, C. Desmedt, G. Gundem, P. Van Loo, T. Aas, L. B. Alexandrov, D. Larsimont, H. Davies, Y. Li, Y. S. Ju, M. Ramakrishna, H. K. Haugland, P. K. Lilleng, S. Nik-Zainal, S. McLaren, A. Butler, S. Martin, D. Glodzik, A. Menzies, K. Raine, J. Hinton, D. Jones, L. J. Mudie, B. Jiang, D. Vincent, A. Greene-Colozzi, P.-Y. Adnet, A. Fatima, M. Maetens, M. Ignatiadis, M. R. Stratton, C. Sotiriou, A. L. Richardson, P. E. Lønning, D. C. Wedge, P. J. Campbell, Subclonal diversification of primary breast cancer revealed by multiregion sequencing. *Nat. Med.* **21**, 751–759 (2015).
29. A. S. Cleary, T. L. Leonard, S. A. Gestl, E. J. Gunther, Tumour cell heterogeneity maintained by cooperating subclones in Wnt-driven mammary cancers. *Nature* **508**, 113–117 (2014).
30. J. H. Brown, J. F. Gillooly, A. P. Allen, V. M. Savage, G. B. West, Toward a metabolic theory of ecology. *Ecology* **85**, 1771–1789 (2004).
31. J. J. Morris, R. E. Lenski, E. R. Zinser, The Black Queen Hypothesis: Evolution of dependencies through adaptive gene loss. *mBio* **3**, e00036-12 (2012).
32. A. Zelezniak, S. Andrejev, O. Ponomarova, D. R. Mende, P. Bork, K. R. Patil, Metabolic dependencies drive species co-occurrence in diverse microbial communities. *Proc. Natl. Acad. Sci. U.S.A.* **112**, 6449–6454 (2015).
33. M.-F. Demierre, P. D. R. Higgins, S. B. Gruber, E. Hawk, S. M. Lippman, Statins and cancer prevention. *Nat. Rev. Cancer* **5**, 930–942 (2005).
34. J. Alizadeh, A. A. Zeki, N. Mirzaei, S. Tewary, A. Rezaei Moghadam, A. Glogowska, P. Nagakannan, E. Eftekharpour, E. Wiechec, J. W. Gordon, F. Y. Xu, J. T. Field, K. Y. Yoneda, N. J. Kenyon, M. Hashemi, G. M. Hatch, S. Hombach-Klonisch, T. Klonisch, S. Ghavami, Mevalonate cascade inhibition by simvastatin induces the intrinsic apoptosis pathway via depletion of isoprenoids in tumor cells. *Sci. Rep.* **7**, 44841 (2017).
35. R. Tsoi, F. Wu, C. Zhang, S. Bewick, D. Karig, L. You, Metabolic division of labor in microbial systems. *Proc. Natl. Acad. Sci. U.S.A.* **115**, 2526–2531 (2018).
36. M. J. I. Muller, B. I. Neugeboren, D. R. Nelson, A. W. Murray, Genetic drift opposes mutualism during spatial population expansion. *Proc. Natl. Acad. Sci. U.S.A.* **111**, 1037–1042 (2014).
37. C. D. Nadell, K. R. Foster, J. B. Xavier, Emergence of spatial structure in cell groups and the evolution of cooperation. *PLOS Comput. Biol.* **6**, e1000716 (2010).
38. J. Calbo, E. van Montfort, N. Proost, E. van Drunen, H. B. Beverloo, R. Meuwissen, A. Berns, A functional role for tumor cell heterogeneity in a mouse model of small cell lung cancer. *Cancer Cell* **19**, 244–256 (2011).
39. N. Aceto, A. Bardia, D. T. Miyamoto, M. C. Donaldson, B. S. Wittner, J. A. Spencer, M. Yu, A. Pely, A. Engstrom, H. Zhu, B. W. Brannigan, R. Kapur, S. L. Stott, T. Shioda, S. Ramaswamy, D. T. Ting, C. P. Lin, M. Toner, D. A. Haber, S. Maheswaran, Circulating tumor cell clusters are oligoclonal precursors of breast cancer metastasis. *Cell* **158**, 1110–1122 (2014).

40. A. K. Casasent, A. Schalck, R. Gao, E. Sei, A. Long, W. Pangburn, T. Casasent, F. Meric-Bernstam, M. E. Edgerton, N. E. Navin, Multiclonal invasion in breast tumors identified by topographic single cell sequencing. *Cell* **172**, 205–217.e12 (2018).
41. X. Jin, Z. Demere, K. Nair, A. Ali, G. B. Ferraro, T. Natoli, A. Deik, L. Petronio, A. A. Tang, C. Zhu, L. Wang, D. Rosenberg, V. Mangena, J. Roth, K. Chung, R. K. Jain, C. B. Clish, M. G. Vander Heiden, T. R. Golub, A metastasis map of human cancer cell lines. *Nature* **588**, 331–336 (2020).
42. P. Dey, J. Li, J. Zhang, S. Chaurasiya, A. Strom, H. Wang, W. T. Liao, F. Cavallaro, P. Denz, V. Bernard, E. Y. Yen, G. Genovese, P. Gulhati, J. Liu, D. Chakravarti, P. Deng, T. Zhang, F. Carbone, Q. Chang, H. Ying, X. Shang, D. J. Spring, B. Ghosh, N. Putluri, A. Maitra, Y. A. Wang, R. A. DePinho, Oncogenic KRAS-driven metabolic reprogramming in pancreatic cancer cells utilizes cytokines from the tumor microenvironment. *Cancer Discov.* **10**, 608–625 (2020).
43. M. Y. Fong, W. Zhou, L. Liu, A. Y. Alontaga, M. Chandra, J. Ashby, A. Chow, S. T. O'Connor, S. Li, A. R. Chin, G. Somlo, M. Palomares, Z. Li, J. R. Tremblay, A. Tsuyada, G. Sun, M. A. Reid, X. Wu, P. Swiderski, X. Ren, Y. Shi, M. Kong, W. Zhong, Y. Chen, S. E. Wang, Breast-cancer-secreted miR-122 reprograms glucose metabolism in premetastatic niche to promote metastasis. *Nat. Cell Biol.* **17**, 183–194 (2015).
44. L. G. T. Morris, N. Riaz, A. Desrichard, Y. Senbabaoglu, A. A. Hakimi, V. Makarov, J. S. Reis-Filho, T. A. Chan, Pan-cancer analysis of intratumor heterogeneity as a prognostic determinant of survival. *Oncotarget* **7**, 10051–10063 (2016).
45. M. Jamal-Hanjani, G. A. Wilson, N. McGranahan, N. J. Birkbak, T. B. K. Watkins, S. Veeriah, S. Shafi, D. H. Johnson, R. Mitter, R. Rosenthal, M. Salm, S. Horswell, M. Escudero, N. Matthews, A. Rowan, T. Chambers, D. A. Moore, S. Turajlic, H. Xu, S.-M. Lee, M. D. Forster, T. Ahmad, C. T. Hiley, C. Abbosh, M. Falzon, E. Borg, T. Marafioti, D. Lawrence, M. Hayward, S. Kolvekar, N. Panagiotopoulos, S. M. Janes, R. Thakrar, A. Ahmed, F. Blackhall, Y. Summers, R. Shah, L. Joseph, A. M. Quinn, P. A. Crosbie, B. Naidu, G. Middleton, G. Langman, S. Trotter, M. Nicolson, H. Remmen, K. Kerr, M. Chetty, L. Gomersall, D. A. Fennell, A. Nakas, S. Rathinam, G. Anand, S. Khan, P. Russell, V. Ezhil, B. Ismail, M. Irvin-Sellers, V. Prakash, J. F. Lester, M. Kornaszewska, R. Attanoos, H. Adams, H. Davies, S. Dentro, P. Taniere, B. O'Sullivan, H. L. Lowe, J. A. Hartley, N. Iles, H. Bell, Y. Ngai, J. A. Shaw, J. Herrero, Z. Szallasi, R. F. Schwarz, A. Stewart, S. A. Quezada, J. Le Quesne, P. Van Loo, C. Dive, A. Hackshaw, C. Swanton; TRACERx Consortium, Tracking the evolution of non-small-cell lung cancer. *N. Engl. J. Med.* **376**, 2109–2121 (2017).
46. S. Li, F. E. Garrett-Bakelman, S. S. Chung, M. A. Sanders, T. Hricik, F. Rapaport, J. Patel, R. Dillon, P. Vijay, A. L. Brown, A. E. Perl, J. Cannon, L. Bullinger, S. Luger, M. Becker, I. D. Lewis, L. B. To, R. Delwel, B. Lowenberg, H. Dohner, K. Dohner, M. L. Guzman, D. C. Hassane, G. J. Roboz, D. Grimwade, P. J. M. Valk, R. J. D'Andrea, M. Carroll, C. Y. Park, D. Neuberg, R. Levine, A. M. Melnick, C. E. Mason, Distinct evolution and dynamics of epigenetic and genetic heterogeneity in acute myeloid leukemia. *Nat. Med.* **22**, 792–799 (2016).
47. C. A. Lyssiotis, A. C. Kimmelman, Metabolic interactions in the tumor microenvironment. *Trends Cell Biol.* **27**, 863–875 (2017).
48. D. Panigrahy, M. L. Edin, C. R. Lee, S. Huang, D. R. Bielenberg, C. E. Butterfield, C. M. Barnes, A. Mammoto, T. Mammoto, A. Luria, O. Benny, D. M. Chaponis, A. C. Dudley, E. R. Greene, J.-A. Vergilio, G. Pietramaggiori, S. S. Scherer-Pietramaggiori, S. M. Short, M. Seth, F. B. Lih, K. B. Tomer, J. Yang, R. A. Schwendener, B. D. Hammock, J. R. Falck, V. L. Manthati, D. E. Ingber, A. Kaipainen, P. A. D'Amore, M. W. Kieran, D. C. Zeldin, Epoxyeicosanoids stimulate multiorgan metastasis and tumor dormancy escape in mice. *J. Clin. Invest.* **122**, 178–191 (2012).
49. I. Spiteri, G. Caravagna, G. D. Cresswell, A. Vatsiou, D. Nichol, A. Acar, L. Ermini, K. Chkhaidze, B. Werner, R. Mair, E. Brognaro, R. G. W. Verhaak, G. Sanguinetti, S. G. M. Piccirillo, C. Watts, A. Sottoriva, Evolutionary dynamics of residual disease in human glioblastoma. *Ann. Oncol.* **30**, 456–463 (2019).
50. P. Kreuzaler, Y. Panina, J. Segal, M. Yuneva, Adapt and conquer: Metabolic flexibility in cancer growth, invasion and evasion. *Mol. Metab.* **33**, 83–101 (2020).
51. F. Dupuy, S. Tabaries, S. Andrzejewski, Z. Dong, J. Blagih, M. G. Annis, A. Omeroglu, D. Gao, S. Leung, E. Amir, M. Clemons, A. Aguilar-Mahecha, M. Basik, E. E. Vincent, J. St-Pierre, R. G. Jones, P. M. Siegel, PDK1-dependent metabolic reprogramming dictates metastatic potential in breast cancer. *Cell Metab.* **22**, 577–589 (2015).
52. F. Roshanzamir, J. L. Robinson, D. Cook, M. H. Karimi-Jafari, J. Nielsen, Metastatic triple negative breast cancer adapts its metabolism to destination tissues while retaining key metabolic signatures. *Proc. Natl. Acad. Sci. U.S.A.* **119**, e2205456119 (2022).
53. J. A. Aguirre-Ghiso, Models, mechanisms and clinical evidence for cancer dormancy. *Nat. Rev. Cancer* **7**, 834–846 (2007).
54. A. D. Hartkopf, F.-A. Taran, M. Wallwiener, C. Hagenbeck, C. Melcher, N. Krawczyk, M. Hahn, D. Wallwiener, T. Fehm, The presence and prognostic impact of apoptotic and nonapoptotic disseminated tumor cells in the bone marrow of primary breast cancer patients after neoadjuvant chemotherapy. *Breast Cancer Res.* **15**, R94 (2013).
55. Z. Hu, Z. Li, Z. Ma, C. Curtis, Multi-cancer analysis of clonality and the timing of systemic spread in paired primary tumors and metastases. *Nat. Genet.* **52**, 701–708 (2020).
56. J. Schindelin, I. Arganda-Carreras, E. Frise, V. Kaynig, M. Longair, T. Pietzsch, S. Preibisch, C. Rueden, S. Saalfeld, B. Schmid, J. Y. Tinevez, D. J. White, V. Hartenstein, K. Eliceiri, P. Tomancak, A. Cardona, Fiji: An open-source platform for biological-image analysis. *Nat. Methods* **9**, 676–682 (2012).
57. D. R. Stirling, M. J. Swain-Bowden, A. M. Lucas, A. E. Carpenter, B. A. Cimini, A. Goodman, CellProfiler 4: Improvements in speed, utility and usability. *BMC Bioinformatics* **22**, 433 (2021).
58. P. A. Ewels, A. Peltzer, S. Fillinger, H. Patel, J. Alneberg, A. Wilm, M. U. Garcia, P. Di Tommaso, S. Nahnsen, The nf-core framework for community-curated bioinformatics pipelines. *Nat. Biotechnol.* **38**, 276–278 (2020).
59. A. Dobin, C. A. Davis, F. Schlesinger, J. Drenkow, C. Zaleski, S. Jha, P. Batut, M. Chaisson, T. R. Gingeras, STAR: Ultrafast universal RNA-seq aligner. *Bioinformatics* **29**, 15–21 (2013).
60. R. Patro, G. Duggal, M. I. Love, R. A. Irizarry, C. Kingsford, Salmon provides fast and bias-aware quantification of transcript expression. *Nat. Methods* **14**, 417–419 (2017).
61. M. I. Love, W. Huber, S. Anders, Moderated estimation of fold change and dispersion for RNA-seq data with DESeq2. *Genome Biol.* **15**, 550 (2014).
62. S. Hanzelmann, R. Castelo, J. Guinney, GSVA: Gene set variation analysis for microarray and RNA-seq data. *BMC Bioinformatics* **14**, 7 (2013).
63. A. Cattaneo, G. Martano, U. Restuccia, L. Tronci, M. Bianchi, A. Bachi, V. Matafora, Opti-nQL: An optimized, versatile and sensitive nano-LC method for MS-based lipidomics analysis. *Metabolites* **11**, 720 (2021).

Acknowledgments: We thank M. Riboni for cDNA preparation, Z. Lavagnino and F. Casagrande for imaging support, and M. Crestani for support in the quantification of circularity. We also thank G. Scita and S. Polo for critical reading of the manuscript. **Funding:** This work was supported by the Climbers Against Cancer Fellowship (B.J.H.), Associazione Italiana per la Ricerca sul Cancro AIRC Pre-Doctoral Fellowship no. 28149 (G.F.), Associazione Italiana per la Ricerca sul Cancro AIRC IG grant no. 23258 (M.C.L. and L.C.), Fondazione Umberto Veronesi (S.P.), and IFOM-ETS Intramural funding. **Author contributions:** Conceptualization: M.C.L., K.R.P., and K.M.H. Investigation: B.J.H. Methodology: B.J.H., S.B., F.O., F.I., S.K., V.M., F.P., G.F., G.S., M.G.T., P.M., and R.G. Data analysis and modeling: F.I., S.M., L.C., and M.C.L. Imaging analysis: P.M., E.M., F.O., S.B., S.M., and B.J.H. Supervision: D.P., A.B., M.C.L., K.R.P., and K.M.H. Data curation: B.J.H. and K.M.H. Writing—original draft: K.M.H. Writing—reviewing and editing: B.J.H., M.C.L., K.R.P., and K.M.H. **Competing interests:** The authors declare that they have no competing interests. **Data and materials availability:** RNA-seq data have been deposited to Gene Expression Omnibus (GEO) with acquisition number GSE223348. All data needed to evaluate the conclusions in the paper are present in the paper and/or the Supplementary Materials.

Submitted 2 March 2023
Accepted 14 August 2023
Published 15 September 2023
10.1126/sciadv.adh4184